

**PROBING THE SURROUNDINGS OF QUANTUM DOTS WITH NITROXIDE
RADICALS**

By

Jeffrey Warren Sayen

A THESIS

Submitted to

**Michigan State University
in partial fulfillment of the requirements
for the degree of**

Chemistry - Master of Science

2015

ABSTRACT

PROBING THE SURROUNDINGS OF QUANTUM DOTS WITH NITROXIDE RADICALS

By

Jeffrey Warren Sayen

This thesis examines the surface chemistry of the CdTe quantum dots by introducing a two unique classes of nitroxide radicals into its chemical environment. Nitronyl and imino nitroxide radicals were strategically chosen as the nitroxide radicals for this study for two reasons. One, each radical has its own unique electronic structure. Two, each radical is known to be chemically stable. CdTe quantum dot system was chosen because of the ease of its synthesis and also their post synthetic flexibility. The synthesis and characterization CdTe quantum dots as well as nitronyl nitroxide and imino nitroxide radicals will be discussed. The chemical interactions of both radicals with the surfaces of the CdTe quantum dots will be also be examined. This includes their potential use as radical ligands for studying the potential binding interactions of both radicals onto the surfaces of the quantum dot. In addition to this, their chemical liability towards the quantum dot and the ligands surrounding the quantum structure will also be discussed. In both studies will be probed with electron paramagnetic resonant spectroscopy.

ACKNOWLEDGEMENTS

I would like to thank my thesis advisor, Dr. Remi Beaulac. He has guided my research efforts for my three-year tenure at MSU as a graduate student. His knowledge of chemistry is vast and his advice is and will always continue to be much appreciated.

I would also like to thank my committee members: Dr. Mitch Smith, Dr. Thomas Hamann, and Dr. Gary Blanchard. Thank you for your help, guidance, and support. I sincerely thank you for being patient with me during a difficult period in my life. It means a lot and is very moving and supportive of my goals in overcoming this huge obstacle in my life.

I would also like to recognize and thank my group members. I will never forget the long hours in the wet chemistry lab or the instrumentation room. I want to thank you so much for helping me navigate the complicated computer programs, which is seemingly becoming more and more difficult as I get older.

Last, I want to thank all my friends and family. To my parents, I want to say thank you for being so there when I needed emotional support and overcoming many of the life challenges which I ran into in graduate school. To my Fiancé, I want to extend to you, the same thanks that I mentioned above to my parents, but additionally I want to add that I love you and I look forward to spending many more years together.

TABLE OF CONTENTS

LIST OF FIGURES	iv
LIST OF SCHEMES	vii
KEY TO ABBREVIATIONS	viii
Chapter 1 Introduction.....	1
1.1 Introduction to Quantum Dots.....	1
1.2 Background to Quantum Dots.....	2
1.3 Physical Properties of Quantum Dots.....	4
1.4 Ligand Dynamics with Ground State Spectroscopy.....	8
1.5 Introduction to Nitronyl and Imino Nitroxide Radicals	11
1.6 Electronic Structure of Nitronyl and Imino Nitroxide Radicals	11
1.7 Coordination Chemistry of Nitronyl and Imino Nitroxide Radicals	16
APPENDIX	20
LITERATURE CITED	27
Chapter 2 Synthesis and Characterization	33
2.1 General Considerations	33
2.2 CdTe Quantum Dot Synthesis and Characterization	34
2.3 Synthesis of NITPh and IMIPh	36
2.4 Conclusions	40
LITERATURE CITED	41
Chapter 3 EPR Spectroscopy of NITPh/IMIPh and CdTe QDs	43
3.1 Introduction	43
3.2 Experimental	46
3.3 Results and Discussion.....	49
3.4 Conclusion	60
APPENDIX	63
LITERATURE CITED	66
Chapter 4 Conclusion	68

LIST OF FIGURES

- Figure 1.1** Representation of the physical changes in the electronic band structure and photo-physics in going from bulk semiconductors to strongly confined QDs. a) Shows the continuous and delocalized orbitals of the conduction and valence bands, separated by the band gap in both bulk semiconductors and QDs. b) Shows the electron and hole picture of the energy levels of a strongly confined QD. The solid circle represents the photoexcited electron; the open circle represents the resulting hole. c) Shows the excitonic states of a quantum confined semiconductor nanocrystal where, $|g, e, b, t\rangle$ are the ground, exciton, biexciton, and triexciton states respectively. 5
- Figure 1.2** The general chemical structures of Nitronyl (Left) and Imino (Right) Nitroxide radicals. 11
- Figure 1.3** The molecular orbital diagram of a nitroxide (N-O) radical, formed from the linear combination of atomic orbitals. 13
- Figure 1.4** The relevant out of plane π -molecular orbital diagram of nitronyl nitroxide. The electron resides in the SOMO which has more π^* -anti-bonding character and is separated by a node on the central sp^2 hybridized carbon..... 14
- Figure 1.5** The relevant out of the plane π -molecular-orbital diagram imino nitroxide radicals. The electron resides in the SOMO which has more π^* -anti-bonding character and is separated by two nodes, one between the nitroxide bond and the other is most likely between the imine nitrogen and the central carbon... 16
- Figure 1.6** The valence bond description of the two tautomer's of the nitroxide bond carrying the unpaired electron. 18

Figure 2.1

The adsorption profile of the first excitonic peak used to calculate the relative diameter and concentration of a CdTe sample. ($D = 3.2$ nm, Concentration = $5.80 \mu\text{M}$)..... 35

Figure 3.1

a) The hydroxylamino anion, nitroxide radical, and nitrosonium cation group. b) A two-electron reduction of nitronyl nitroxide yields imino nitroxide. A three electron reduction results in two tautomers: amidino and the hydroxylamino which are in equilibrium. 45

Figure 3.2

a) CW-EPR spectra of $100 \mu\text{M}$ of NITPh in distilled and de-aerated Toluene. b) The g_{iso} values of NITPh as calculated from the center inflection line of spectrum a. c) CW-EPR Spectra of $100 \mu\text{M}$ of IMIPh in distilled and de-aerated Toluene. d) The g_{iso} values of IMIPh as calculated from the center inflection line of spectrum c. 49

Figure 3.3

a) Room Temperature CW-EPR Spectra of $100 \mu\text{M}$ NITPh: $1 \mu\text{M}$ CdTe ($D = 3.6$ nm) in de-aerated toluene. b) The normalized total integrated intensity of $100 \mu\text{M}$ NITPh and $1 \mu\text{M}$ CdTe ($D = 3.6$ nm) given in a. c) Room Temperature CW-EPR Spectra of $200 \mu\text{M}$ NITPh and $1 \mu\text{M}$ CdTe ($D = 3.5$ nm) in de-aerated toluene. d) The normalized total integrated intensity of $200 \mu\text{M}$ NITPh and $1 \mu\text{M}$ CdTe ($D = 3.6$ nm) given in c..... 51

Figure 3.4

a) Room Temperature CW-EPR Spectra of $100 \mu\text{M}$ IMIPh and $1 \mu\text{M}$ CdTe ($D = 3.6$ nm) in distilled and de-aerated toluene. b) The normalized total integrated intensity of $100 \mu\text{M}$ IMIPh and $1 \mu\text{M}$ CdTe ($D = 3.6$ nm) given in a. c) Room Temperature CW-EPR Spectra of $200 \mu\text{M}$ IMIPh and $1 \mu\text{M}$ CdTe ($D = 3.4$ nm) in de-aerated toluene. d) The normalized total integrated intensity of $200 \mu\text{M}$ IMIPh and $1 \mu\text{M}$ CdTe ($D = 3.4$ nm) given in c. 53

Figure 3.5

a) Room Temperature CW-EPR Spectra of $100 \mu\text{M}$ NITPh and $1 \mu\text{M}$ CdTe ($D = 3.5$ nm) whose ligands have been exchanged with octadecylamine, in de-aerated toluene. b) The normalized total integrated intensity of $100 \mu\text{M}$ NITPh and $1 \mu\text{M}$ CdTe ($D = 3.5$ nm) given in a. c) Room Temperature CW-EPR Spectra of $100 \mu\text{M}$ IMIPh and $1 \mu\text{M}$ CdTe ($D = 3.5$ nm) whose ligands have been exchanged with octadecylamine, in de-aerated toluene. d) The

normalized total integrated intensity of 100 μ M IMIPh and 1 μ M CdTe (D = 3.5 nm) given in c. 57

Figure 3.6

a) Room Temperature CW-EPR Spectra of 100 μ M NITPh and 100 μ M trioctylphosphine in de-aerated toluene b) The normalized total integrated intensity of 100 μ M NITPh 100 μ M TOP given in a. 60

Figure A.1

31 P NMR spectra of CdTe (D = 3.5 nm) prior too (top) and following (bottom) the ligand exchange procedure..... 64

Figure A.2

Normalized Absorbance spectra of CdTe (D = 3.5nm) prior too (14.5 μ M - red) and following (500 nM - blue) the ligand exchange procedure. 65

LIST OF SCHEMES

Scheme 2.1	The general reaction scheme of NITPH and IMIPh.	36
-------------------	--	----

KEY TO ABBREVIATIONS

ΔB	Line Width Peak-to-Peak in Gauss
a	Hyperfine Splitting Value
CW-EPR	Continuous Wave-Electron Paramagnetic Resonance
D	Diameter of Quantum Dot
EPR	Electron Paramagnetic Resonance
ESI-MS	Electron Spray Ionization-Mass Spectroscopy
G	Gauss
g_{iso}	Isotropic g Value
HOMO	Highest Occupied Molecular Orbital
I	Signal Intensity
IMI	Imino Nitroxide
IR	Infrared Spectroscopy
LUMO	Lowest Unoccupied Molecular Orbital
lwpp	Line Width Peak-to-Peak
m.p.	Melting Point
NIT	Nitronyl Nitroxide
NIR	Near Infrared Spectroscopy
NMR	Nuclear Magnetic Resonance
N-O	Nitroxide Bond
Ph	Phenyl
PL	Photoluminescence
QD	Quantum Dot
SOMO	Single Occupied Molecular Orbital
T_2	Spin-Spin Relaxation
TLC	Thin Layer Chromatography
UV-VIS	Ultraviolet-Visible Spectroscopy

Chapter 1

Introduction

1.1 Introduction to Quantum Dots

Quantum dots (QD) are semiconductor nanocrystals with dimensions on the order of a few to several hundred nanometers. Nanocrystal semiconductors, unlike bulk semiconductors, exhibit atomic-like optical properties as a result of their size. Furthermore the influence of these properties scales with the size of the nanocrystal and are therefore size-dependent.¹⁻² Colloidal QDs are among the most investigated semiconductor nanocrystals because of their high luminescence efficiency, tunable emission spectra over a wide spectral range, and their abnormally long photo-excited lifetimes. A few promising applications for QD include color enhanced light emitting diodes, energy efficient lasers, fluorescent biochemical sensors, and as light and charge carriers in photovoltaic cells.³⁻⁷

In the past it was commonly believed that the size of the QD was the most dominant feature governing the final optical properties of the QD. However, the results from a variety of different researcher efforts indicate the ligands surrounding the QD may also have a strong influence. Furthermore, it is increasingly becoming clear that these influences are strongly dependent on the physiochemical properties of these ligands. There is even some evidence that they maybe be able to participate in excited-state electron transfer processes, and can act as donors/acceptors species.⁴ This has exciting implications for both the present and future applications of QDs.

1.2 Background to Quantum Dots

Colloidal semiconductor nanocrystals are composed of a nanoscale semiconductor core surrounded by a shell of organic ligand molecules. The optical and material properties of a semiconductor nanocrystal can be considered as an intermediate regime between that of a small molecule and that of a bulk semiconductor as a result of their decreased dimensions. In bulk semiconductors, the dimensions of the system are essentially infinite compared to the dimensions of the carriers, electrons, and holes. In these bulk systems the wave functions are considered as standing waves within the material, which are spread over an almost infinite number of unit cells. The resulting density of states is essentially continuous throughout the bulk crystals lattice except in the region of the band gap of the semiconductor. When the bulk semiconductor is confined to the nano-scale regime the once continuous boundary conditions of the wave function becomes confined.¹

As the boundary conditions associated with the wave functions become confined, the density of states within the crystal begins to change from a continuous model to a more discrete model. In this confinement regime the nanocrystal behaves more like a small molecule and this effect is analogous to a particle in a box model in quantum mechanics. The physical dimensions required to spatially confine the electron or hole depend on the size of the electron and hole wave functions, which is an intrinsic physical property of a given material. If the semiconductor crystals dimensions are significantly larger than the electron and hole wave functions, it is expected to have more bulk like properties. The determining factor between these two size regimes is largely left to the degree of confinement of the wave functions relative to the size of the nanocrystal.

Quantum confined semiconductor nanocrystal have been widely studied for the past three decades due to their size tuneable optical properties and unique physical characteristics. This

area of research was founded in the late 1970s and early 1980s when researchers at Bell Laboratories and the Yoffe Institute independently described the properties of nanometer sized quantum confined semiconductor crystals found in the structural defects of semiconductor-doped glasses. These early semiconducting materials were problematic to study because they often displayed large inhomogeneous size distributions and poor synthetic control over crystalline growth factors. Early attempts at synthesizing dispersed colloidal nanocrystals were also plagued by poor control of size distribution due to problems with initiating growth factors such as nucleation and surface passivation.

In the early 1990s a new synthetic procedure was developed so that the nucleation and growth of colloidal nanocrystals could be reproducibly controlled. This was achieved by injecting highly reactive organometallic precursors in a solvent system and using temperature control to induce colloidal growth. This technique is commonly referred to as the hot injection method. The hot injection method is the most commonly used synthetic technique because of its ease, reproducibility, and homogenous particle size control.⁵

Quantum dots synthesized via this route become inorganic/organic hybrid materials where the inorganic core is capped by a monolayer of organic ligands.⁶ Typically the organic capping ligands are chosen to have large HOMO-LUMO gaps, which are used to remove the unsaturated valences associated with dangling bonds on the surface of the nanocrystalline lattice. Furthermore these surface defects are strongly coupled to the photo-physical properties associated with QDs. While the use of capping surface ligands was a milestone in colloidal QDs, they also introduce certain limitations for potential use in key applications. For example, the use of native ligands would not be appropriate for designing a QD system with the eventual goal of

having it participate in photoexcited electron extraction or redox chemistry. To understand why, the photo-physical properties of QDs must also be introduced.

1.3 Physical Properties of Quantum Dots - Adsorption and Photoluminescence

A feature common to all semiconductors is the band gap of the material, which separates the conduction band and the valence band. When a semiconductor adsorbs light, an electron is promoted from the valence band to the conduction band, leaving behind a hole in the valence band that the excited electron previously occupied. The wavelength of the adsorbed and emitted light is determined by the width of the semiconductors band gap.

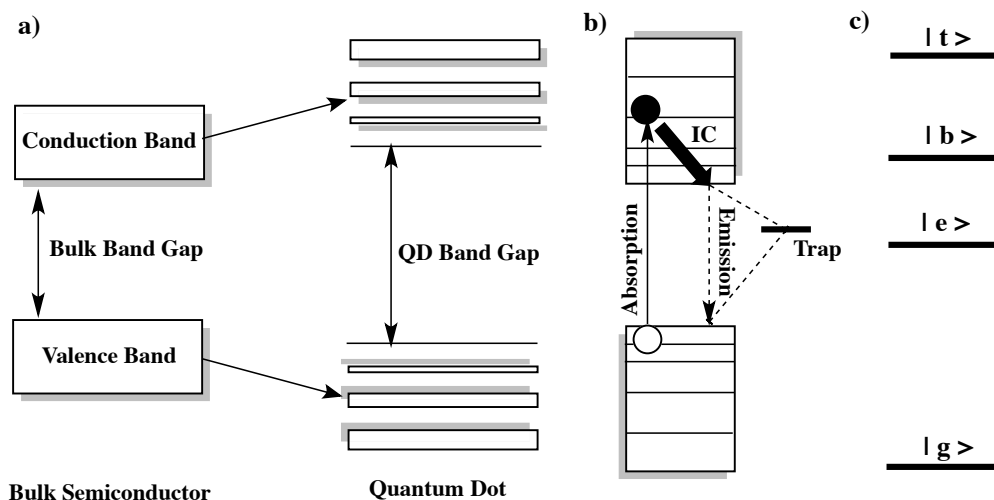
When a semiconductor is excited in a way that decreases the Colombic attraction of a hole and electron an exciton can be created. The spatial extent of the exciton wave function is comparable to that of a hydrogen atom and is described by a quantity called the exciton Bohr radius with the lowest energy states comprised of the bound electron-hole pair. It is these optically active exciton states that adsorb and emit light in a semiconductor. In this way excitons can be thought of as a net neutral charge carrier in a confined semiconductor system.⁷

When the size of the semiconductor approaches the nano-regime, the confinement modifies this Hamiltonian by adding a potential that restricts the spatial distance between an electron and hole. This restricted spatial overlap concentrates the continuous energy bands of the bulk semiconductor and results in a set of high oscillator strength discrete transitions. The position of these states and therefore the adsorption spectra depends on the spatial confinement of the exciton, which is determined by the physical size of the nanocrystal. The physical changes, which occur to the density of states in going from bulk semiconductors to the nanoscale regime, are shown in figure 1.1a.

The energy levels of quantum-confined nanocrystals can be represented in terms of two basic frameworks. These are shown in figure 1.1b and 1.1c. One is modeled closer to that of a bulk system, with separate electron and holes. The other is mapped onto exciton states. Both pictures describe aspects of the physical system, although strictly speaking photo-excitation results in bound excitonic states. However, in certain cases it is easier to visualize the electron and hole as being separate entities. These include processes such as charge separation and localization of the hole on a trap state or relaxation processes that affect the electron and the hole in different ways following dissociation.

Following the photo-excitation of the confined semiconductor nanocrystal system, the exciton can relax through a variety of radiative and non-radiative pathways. The exciton can relax non-radiatively through these levels before returning or recombining with a hole in the ground state, giving the nanoparticle sharp fluorescent properties with high quantum yield.⁸ This is shown in figure 1.1b. While this sort of relaxation can be thought of as an analogy to molecular intersystem crossing, it differs because strongly confined nanocrystals display larger electronic energy spacing than their low frequency vibrational modes. In addition to this, the hole or the electron can migrate to a surface defect site. This acts to quench the exciton and results in lower Quantum Yields. This is also shown in figure 1.1b

Figure 1.1. Representation of the physical changes in the electronic band structure and photo-physics in going from bulk semiconductors to strongly confined QDs. a) Shows the continuous and delocalized orbitals of the conduction and valence bands, separated by the band gap in both bulk semiconductors and QDs b) Shows the electron and hole picture of the energy levels of a strongly confined QD. The solid circle represents the photoexcited electron; the open circle represents the resulting hole. c) Shows the excitonic states of a quantum confined semiconductor nanocrystal where, $|g, e, b, t\rangle$ are the ground, exciton, biexciton, and triexciton states respectively.



It is commonly believed that the surface impurities at the defect sites act as competitive energetic states that trap the exciton within the crystal lattice. Recently however, it has been proposed that organic ligands at the interface of these defect sites can also influence their energetic level, and therefore influence the optical properties of the QD. It is thought that the organic ligands act to donate or withdraw electrons to the dangling bonds which are either electron donating (Se^{2-} , Te^{2-} , etc) or electron withdrawing (Cd^{2+} , Pb^{2+} , etc).^{9,10} For example, trioctylphosphine oxide and trioctylphosphine are typical native ligands used in the hot injection synthesis technique and they typically result in QDs with a fluorescent quantum yield of no more than 5-15%.^{11,12} Furthermore, it has been reported that the addition of hexadecylamine to the precursor mixture can increase the fluorescent QY to about 50% even at room temperature.¹³ Primary alkylamines ligands have been shown to increase the quantum yields associated with photoluminescence when they are added at lower concentrations relative to the QD. However, contrary to this initial increase in photoluminescence at lower concentrations, at higher concentrations they have also been shown to decrease photoluminescent quantum yields.¹⁴⁻¹⁵ In general, studies with alkanethiols tend to enhance photoluminescence, as well as making the QD

soluble polar solvents including water. Both of these features are often desirable based on specific applications for the QD system.¹⁶⁻¹⁷

Interband relaxation from the first excitonic state also has radiative pathways that outcompete non-radiative pathways associated with electron-hole recombination.⁴ In this mechanism electrons or holes are trapped to energetically accessible states, which occur within the QD lattice or on the surface defect sites. Ligands can control the surface traps by determining the oxidation potentials of these atoms.

Surface cations on the QD surface have empty 5s electron-accepting shells (Cd^{2+} , Pb^{2+} , etc), which are expected to mix more readily with σ -donating ligands, because they share the orbitals of similar symmetry.¹⁸ Alkylamine ligands are strong σ -donors which act to increase the photoluminescence intensity of certain QDs.¹⁷ When hexadecylamine is added to CdSe QD systems it increases the PL intensity, but this enhancement in photoluminescence was steadily lost over time as the ligand desorbs from the surface and is rapidly replaced by solvents.¹⁶ Studies on a series of anilines, which varied only by the σ -donating strength of their functional groups, suggested that weaker σ -donating ligands resulted in photoluminescence quenching of CdSe QDs. It was suggested that the weaker σ -donating ligands decrease the electron density at the coordinating surface site. Within the same class of anilines, the stronger σ -donating ligands seemed to have an opposite effect, increasing the electron density of the coordinating surface site and resulting in less quenching of the QD photoluminescence.¹⁸ Other electron donors such as tetradecylphosphonic acid and trioctylphosphine oxide, also increase the photo-luminescent quantum yields of QD.^{16,19} These ligands have the added benefit that they are commonly used in QD synthesis to passivate the QD surface.

In addition to controlling the oxidation state of the surface defect states, it is also commonly thought that σ -donating ligands create an interfacial energy state, which is located in either the valence or conduction band of the semiconductor.¹⁸ This has the effect of removing the thermodynamic trap of the exciton, thereby increasing its chances for relaxation radiatively. Within this model, if the HOMO-LUMO gap overlaps well with the defect state surface metal orbitals, they can couple to and therefore influence the nature of the exciton by creating a new state that energetically lies in the range of the conduction band, valence band, or in between the two.¹⁸ This effectively removes the thermodynamic trap associated with the non-radiative decay pathway, thereby enhancing the radiative pathway. Both σ - and π - donating ligands have also been shown to effect the photoluminescence by forming a hole-trapping state within the electronic structure of the QD.^{19,20}

There is evidence that thiolates may act as a hole trapping ligands, because one lone pair of electrons on the sulphur atom donates to the metal cation while the two other lone pair can act as thermodynamic traps for valence band holes.^{21,22} Depending on the initial surface chemistry of the QDs, the band gap of the QDs, along with the electronic structure of the ligand; the addition of thiolates can either enhance or quench the photoluminescence of the QD.^{19,23,24} The degree to which the thiolate ligand affects the PL is thought to depend on a variety of factors given in the above examples, along with the strength that its chemical structure allows it to bind to the metal cations while still being available to interact with other surface defect sites with its remaining lone pair electrons.

1.4 Ligand Dynamics with Ground State Spectroscopy

The most widely used spectroscopic techniques for studying QDs and QD-ligand systems are steady-state absorption and emission spectroscopy. As was discussed above, the resulting

photoluminescent quantum yield emitted by a QD, depends strongly on the electronic properties of ligand introduced onto its surface. However it also depends on the degree of surface coverage or passivation by the organic ligands, as the binding affinity of the organic ligands will determine the relative passivation and depending on the ligand the degree to which the exciton will decay via a non-radiative pathway.

Since organic "native" ligands are present during QD synthesis, modifying the QD surface by introducing different post synthesis ligands necessitates a need for different forms of spectroscopy in order to accurately characterize the surfaces of the QD. NMR has been used to quantitatively assess surface ligand coverage and ligand exchange procedures. ^{31}P NMR is one of the most widely used NMR techniques for these purposes, since many of the native ligands used in QD synthesis are phosphorus-containing ligands such as trioctylphosphine and trioctylphosphine oxide. Many times it is desirable to remove these native ligands from the QD system in order to enhance the optical properties of the QD.²⁵ ^{31}P NMR is widely used to show the removal of phosphorus containing ligands.

^{31}P NMR can be used to track impurities in the trioctylphosphine and trioctylphosphine oxide ligands. This is important because trioctylphosphine and trioctylphosphine oxide are dynamically bound to the QD surface during and post synthesis.²⁶ Known phosphine impurities such as alkylphosphonate and other phosphine oxides can both influence the nanoparticle size and the resulting ligand shell of the during the synthesis and treatments following the synthesis of QDs.^{25,27,28} This technique is also useful for studying ligand exchange mechanisms, where phosphine ligands are removed and replaced by other surface ligands such as amines or thiols.

^1H NMR has been used to characterize the QD ligands shells with ligands consisting of thiols^{29,30}, amines^{31,32}, and phosphonic acids/oxides^{16,33,34}, and carboxylic acids.³³ In some cases

surface interactions, which result from chemical reactions, are detectable as line width changes or new spectral peak positions associated with the chemical interaction.³⁵ While the majority of these studies were used in conjunction with steady state luminescence to elucidate the binding mechanisms of the ligands to the QD surfaces, certain correlations can be determined. In some cases line width changes and line broadening occur as a result of different binding modes to the QD surface. This measurement can in turn be correlated back to an estimated ratio of bound and unbound chemical ligands. In some studies there is a close agreement between the resultant binding equilibrium between the two spectroscopic techniques, while it can vary considerably in others. Using NMR for quantitative ligand binding studies is difficult because the ligands are known to be in a dynamic state between bound and unbound species which leads to only estimated ratios of the surface bound and unbound ligands.³⁵ Changes in chemical shifts can also indicate QD-facilitated chemical reactions such as the photo-oxidation of thiols to disulfides with CdSe and CdS QD.^{29,36}

There are major challenges associated with using NMR to study the surfaces of QDs. One problem is that the large surface areas associated with the QD are often covered with a large number of coordinating ligand molecules. Furthermore these ligands are not homogenous, and are comprised of a mixture of native ligands and any subsequent ligand introduced into the system. In addition to this, NMR requires a large number of resonating spins, often with concentrations in the millimolar range. This can make distinguishing peak shifts due to ligand-QD surface interactions difficult. Another drawback associated with NMR is that the relaxation times governing line width changes associated with surface-ligand interactions occur on the millisecond to second timescale.³⁷ Very often ligand dynamics in QD systems occur much faster than this making detection very difficult. Because of this, most studies rely on a combination of

steady state luminescence as well as NMR to correlate ligand-binding dynamics in colloidal QDs.³⁵

1.5 Introduction to Nitronyl and Imino Nitroxide Radicals

Nitronyl nitroxides (NIT) and imino nitroxides (IMI) are a class of stable and persistent free radicals, which were developed in the late 1960's and 1970's by E.F. Ullman.^{38,39} Their properties closely resemble those of the well studied Tempo and Proxyl mono-nitroxide radicals. Ullman bi-functionalized the nitroxide groups of these mono-nitroxide radicals across a heterocyclic ring, creating the nitronyl nitroxide radical. Nitronyl nitroxides showed remarkable chemical stability in comparisons to their mono-nitroxide analogues, which themselves are sometimes only moderately stable. Although discovered in the early 1970's, their popularity waned until the early 1990's, when they rapidly found resurgence for potential use as organic-inorganic hybrid molecular magnets.⁴⁰ The general structure of both radicals is shown in figure 1.2.

Figure 1.2. The general chemical structures of Nitronyl (Left) and Imino (Right) Nitroxide radicals.



1.6 Electronic Structure of Nitronyl and Imino Nitroxide radicals

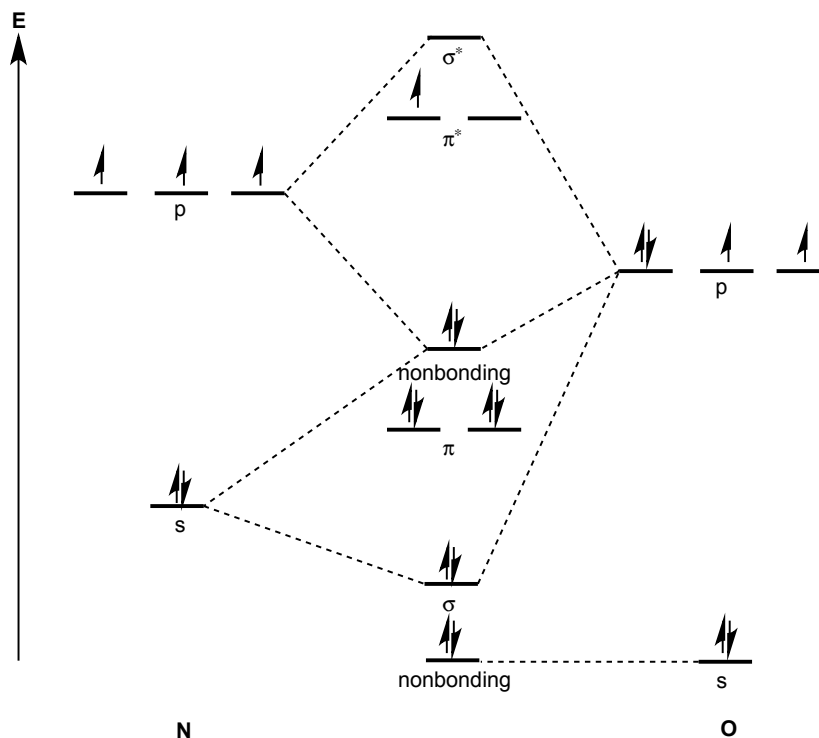
Both nitronyl nitroxide (NIT) radicals and imino nitroxide (IMI) are considered π -type organic radicals as the unpaired electron is delocalized over the π -molecular orbitals of the ONCNO (NIT) and ONCN (IMI) fragments. These fragments, respectively form the backbone of the conjugated heterocyclic ring of both radicals. Both radicals also exhibit a large amount of

spin polarization due to the physical nature of the nitroxide groups found in each radical. The existence of spin polarization in these radicals may be important for their potential use as spin probe molecules for studying the defect sites of Cd based quantum dots.

The electronic structure of both radical's can be rationalized by considering the out of plane p-orbitals. Both radicals are approximately planar, so that the conjugated ring fragment carrying the nitroxide bonds can be considered planar as well. The nitroxide bond (NO) is the most important fragment of both NIT and IMI nitroxides for spin probe application. A description of its electronic structure serves as a good starting points towards this goal.

In terms of valence bond theory, the nitrogen atom of the NO bond can be considered as sp^2 -hybridized while the oxygen can be considered as sp -hybridized. Therefore the frontier p_z atomic orbitals form bonding, non-bonding, and anti-bonding molecular orbitals, and the lone electron gets placed in the anti-bonding orbital. The molecular orbital diagram of a nitroxide N-O bond is depicted below in figure 1.3. In general nitroxide radicals are very sensitive to any environmental perturbations that influence atomic character of the unpaired electron. This is why they are so popularly used as spin probes.

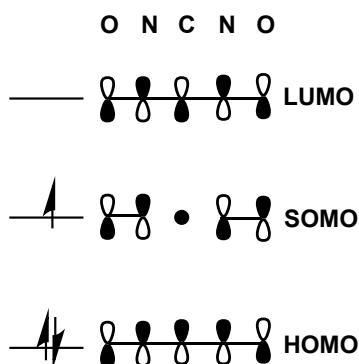
Figure 1.3. The molecular orbital diagram of a nitroxide (N-O) radical, formed from the linear combination of atomic orbitals.



Two nitroxide fragments are bonded through a central sp^2 -hybridized carbon, creating a conjugated O-N-C-N-O fragment that makes up the general heterocyclic ring structure found on nitronyl nitroxide radicals. The nitroxides are bonded to the central carbon through the π^* -molecular orbitals of the nitroxide bond, which themselves carry more atomic nitrogen character. Therefore the ring structure of nitronyl nitroxides can be considered a type of three center-three electron bond having C_2 symmetry. Five molecular orbital energy levels are formed from the linear combination of atomic orbitals (LCAO). In C_{2v} symmetry, two representations transform as A_2 and three transform as B_2 . The central carbon's atomic orbitals do not contribute to the A_2 representation, leaving an odd orbital contribution to the π -molecular orbital structure. This region is often referred to as a node. The most stable ordering of the three electrons in these orbitals is a ground doublet, where the free electron resides in an anti-bonding orbital which is

primarily composed of π^* -nitroxide character delocalized over a nodal region of the central carbon.^{41,42} This frontier molecular orbital is referred too as the singly occupied molecular orbital (SOMO). Following this notation the next lowest energy frontier π -molecular relative to the SOMO is referred to as the SOMO-1 and the highest energetic frontier orbital is referred to as the SOMO+1. The general structure of the π -molecular orbital system for nitronyl nitroxide radicals is shown in figure 1.4.

Figure 1.4. The relevant out of plane π -molecular orbital diagram of nitronyl nitroxide. The electron resides in the SOMO which has more π^* -anti-bonding character and is separated by a node on the central sp^2 hybridized carbon.



The node, which is physically derived from the C_2 symmetry, has very important physical consequences concerning the general electronic structure of nitronyl nitroxides. In addition, in the ground state electron configuration the centralized carbon should be completely void of spin density. However, neutron diffraction studies have proven the existence of negative spin density at central sp^2 hybridized carbon atom.⁴³ The existence of negative spin density at the central carbon is a result of spin polarization.

Spin polarization is a destabilization effect felt by inner-shell electrons as a result of π -spin density of the delocalized unpaired electron. It can contribute both positive and negative nuclear spin densities. In general its contributions are greater when the nucleus is closer too or lies in the nodal plane of the SOMO, however its effects can also propagate over a number of

distant nuclei and is therefore a global effect. Spin polarization is common in many π -type organic radicals, and it has a significant effect on the distribution of spin density and therefore its resulting electronic structure. However, its contribution to nonlocal nuclei depends on the magnitude of its own local π -spin density, which is governed by spin delocalization effects. Spin delocalization contributes positive spin density, and it nominally reflects the spin density of the orbitals containing the unpaired electron.^{44,45}

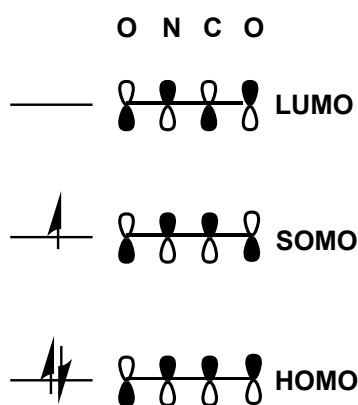
The node also has physical consequences regarding the excited state spectra of nitronyl nitroxide radicals because it implies that constituent groups with available p_z orbitals can only contribute to the SOMO-1 and SOMO+1 orbitals and are isolated from contributing to the SOMO orbital. However, the central carbon does contribute slightly to SOMO because of spin polarization effects.⁴¹

The C_2 symmetry constraints placed on nitronyl nitroxides is lifted in imino nitroxides, and the central carbon atom in the ONCN fragment is no longer necessarily a node. There are actually two nodes present when subtracting an oxygen p_z atomic orbital in forming the molecular orbital of the SOMO. As a result of the disappearance of the node, it may be assumed that positive spin density should be found at the central carbon. However, neutron diffraction studies have confirmed that the spin density remains negative, although it less pronounced than in nitronyl nitroxides.^{46,47} In addition to this, there was a pronounced shift of positive spin density towards the nitroxide (-NO) oxygen, while the imine nitrogen itself retained a substantial amount positive spin density. The absence of spin density at the central carbon is a result of spin polarization.

Assigning the nodes to a qualitative MO picture of imino nitroxides is a bit trickier compared to nitronyl nitroxides. One node clearly belongs to the p_z orbitals of the nitroxide

bond, but the placement of the other is a little more arbitrary. Considering that the imine nitrogen is sp^2 hybridized and still carries positive spin density, the other node probably occurs between itself and the central carbon.⁴² The general structure of the π -molecular orbital system for imino nitroxide radicals is shown in figure 1.5.

Figure 1.5. The relevant out of the plane π -molecular-orbital diagram imino nitroxide radicals. The electron resides in the SOMO which has more π^* -anti-bonding character and is separated by two nodes, one between the nitroxide bond and the other is most likely between the imine nitrogen and the central carbon.



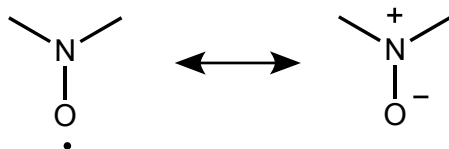
1.7 Coordination Chemistry of Nitronyl and Imino Nitroxide Radicals

The coordination chemistry of nitronyl nitroxides and imino nitroxides is well known, mostly through their use in designing inorganic-organic hybrid molecular magnets.⁴⁰ As ligands, nitronyl nitroxides behave as weak Lewis bases as coordination typically occurs through a lone pair donation at the nitroxide oxygen, forming a typical donor-acceptor dative bond. Their donor strength also depends heavily on the donating properties of their constituent groups, which will preferentially coordinate to the metal center if they carry strong donating groups. Imino nitroxide radicals can also coordinate through their nitroxide bond, however coordination is more likely to occur through the imine nitrogen as it is a slightly stronger Lewis base.⁴⁸ As with nitronyl nitroxide radicals, preferential coordination to the metal center occurs through constituent group if they carry an additional functionalized donor group.

One of the most important physical properties found in most nitroxide-metal complexes is that the nitroxide ligands retains its unpaired spin density upon coordination, thereby retaining its radical character. This is one of the reasons nitronyl nitroxides and imino nitroxide radicals have traditionally been the radicals of choice in designing molecular magnets. It is also the reason why mono-nitroxide radicals have traditional been used for spin probe applications. Regardless of the application, most of the previous research regarding nitroxide complexes has primarily been focused on the paramagnetic metal centers.⁴⁹ Despite this, there have been a few studies involving metal ligand with diamagnetic metal centers. A few of these include: AlCl_3 , BCl_3 , SnCl_4 , SnBr_4 , SiF_4 , SiCl_4 , $\text{Ti}(\text{OPh})_4$, complexed to mono-nitroxide ligands, as well as $\text{Hg}(\text{NO}_3)_2$, $\text{Zn}(\text{NO}_3)_2$, $\text{Cd}(\text{NO}_3)_2$, $\text{Ag}(\text{NO}_3)_2$, and $\text{Pb}(\text{NO}_3)_2$ complexed to nitronyl and imino nitroxide ligands.^{48,50}

Metal-nitroxide radical complexes studied with EPR spectroscopy attempt to correlate the changes in the hyperfine coupling constants, which occurs as a result of the changes in spin density upon complex formation. The changes in the electronic structure of nitroxide radicals upon complex formation are best understood by considering two resonance structures of a nitroxide bond. Both of these tautomers are shown in Figure 1.6. Both resonant forms account for the spin delocalization effects found in nitronyl and imino nitroxide radicals. However, upon complex formation, the nitroxide oxygen donates two pairs of electron, which subsequently acts to increase its electronegativity. To stabilize the formal charge on nitrogen, the resonance structure on the right becomes favored.⁵¹ The valence bond description can also be rationalized in terms of molecular orbital theory. Coordination causes the unpaired electron to localize on the p_z orbital of the nitrogen atom as a result of paired electrons localizing on the p_{xx} orbitals of the oxygen atom.

Figure 1.6. The valence bond description of the two tautomer's of the nitroxide bond carrying the unpaired electron.



The changes that occur to the electronic structure of the nitroxide radical upon metal complex formation have been confirmed with high-resolution spin density maps using polarized neutron diffraction experiments.⁵⁰⁻⁵² The molecular orbital picture is more convenient for EPR applications, because it involves a shift in spin density towards the nitroxide nitrogen, which is directly related to the ^{14}N hyperfine-coupling constant. The same electronic changes that occur in nitronyl nitroxide radicals at the nitroxide nitrogen, also occur in imino nitroxide radicals at the imine nitrogen. Coordination at the imine nitrogen also causes an increase in the ^{14}N hyperfine-coupling constant as a result of charge being pulled towards the coordinating imine nitrogen by an inductive effect. As a result of these changes, the strength of the coordination bond at either the nitroxide oxygen or the imine nitrogen are proportional to observed increase in the hyperfine-coupling constant. If coordination of either nitronyl or imino nitroxide radicals to the surface of the QD occurs, it is expected that will donate their valence electrons to the Cd^{2+} surface ions.

The primary goals of this thesis are two fold. One, is to synthesis a related class of nitronyl and imino nitroxide radicals as well as samples of CdTe QDs within a consistent diameter range. This is the subject of chapter 2. The other goal of this thesis is to attempt to use EPR to study the probe the interactions of both radicals with the surfaces of the synthesized QDs. These interactions include the radical binding to the surface of the QD, or any subsequent reactions the radical may undergo with either the QDs themselves, the QDs surrounding ligands,

or a combination of both. This will be the subject of chapter 3. For a brief familiarization with the basics of EPR spectroscopy as it relates to both nitroxide radicals, the reader is directed towards the appendix at the end of this chapter.

APPENDIX

Appendix

Basics of Electron Paramagnetic Resonance

Electron Paramagnetic Resonance or EPR is a spectroscopic method relying a purely quantum mechanical construct of the electron spin. The spin Hamiltonian is a linear function of the applied magnetic field, with operators:

$$\hat{H} = \hat{H}_{EZ} + \hat{H}_{HFS} + \hat{H}_{NZ} + \dots \quad (\text{B.1.1})$$

Each operation will result in eigen values which contribute to the total energy of the spin system. The terms describe the electron Zeeman interaction (\hat{H}_{EZ}), the nuclear Zeeman interactions (\hat{H}_{NZ}), and the hyperfine coupling interaction between the electron spin and the nuclear spin (\hat{H}_{HF}). There are other contributing interactions that make up the total spin Hamiltonian of general spin systems, but these have been omitted for the purposes of this thesis because they have a negligible contribution with regards to nitroxide radicals. These lesser contributing terms to the overall spin Hamiltonian include zero field splitting effects, the nuclear quadrupolar interactions for spin $I > 1/2$, and spin spin-spin interactions between pairs of nuclear spins. Since the spin Hamiltonian is separated by energy contributions, it is reasonable to ignore them for nitroxide radicals as these interactions have negligible energetic contributions.

The interaction between the electron spin and the external magnetic field is described by the electron Zeeman term:

$$\hat{H} = \mu_B \mathbf{S} \cdot \mathbf{g} \cdot \mathbf{B}_0^T \quad (\text{B.1.2})$$

Since both the spin operator \mathbf{S} and the external magnetic field \mathbf{B}_0 are explicitly orientation-dependent with respect to their interaction with paramagnetic species, \mathbf{g} assumes the form of a tensor. The tensor is described with the components:

$$\mathbf{g} = \begin{pmatrix} g_{xx} & g_{xy} & g_{xz} \\ g_{yx} & g_{yy} & g_{yz} \\ g_{zx} & g_{zy} & g_{zz} \end{pmatrix} \quad (\text{B.1.3})$$

The deviation of the \mathbf{g} principal values from the g_e value of the free electron spin and its orientation dependence is caused by spin-orbit coupling. Since the orbital angular momentum \mathbf{L} is quenched for a non-degenerate ground state, only the interaction of the excited states and ground state leads to an admixture of the orbital angular momentum to the spin angular momentum. The \mathbf{g} tensor can also be expressed by:

$$\mathbf{g} = g_e \mathbf{1} + 2D\mathbf{\Lambda} \quad (\text{B.1.4})$$

where D is the spin-orbit coupling constant and $\mathbf{\Lambda}_{ij}$ is a symmetric tensor with elements:

$$\Lambda_{ij} = \sum_n \frac{\langle \psi_0 | L_i | \psi_n \rangle \langle \psi_n | L_j | \psi_0 \rangle}{\epsilon_0 - \epsilon_n} \quad (\text{B.1.5})$$

Each element Λ_{ij} describes the interactions of the SOMO ground state ψ_0 with the energy ϵ_0 and the n th excited state ψ_n with energy ϵ_n . A large deviation from g_e can result from a small energy difference between the SOMO and the lowest excited state and/or large spin-orbit coupling values. Large deviations from the value of g_e are observed for transition metal complexes, and for most organic radicals, the excited states are high in energy and $g_{ij} \approx g_e$. Nitroxides show a slight deviation from the g_e due to spin orbit coupling in excited states that involve the lone pair orbitals on oxygen.

The \mathbf{g} tensor can be simplified by a series of Euler angle transformations, based on the symmetry of the molecule. This involves the orientation of the molecule with respect to the magnetic field vector. A principal axes system can be chosen to coincide with three unique orthogonal axes, which is dictated by the symmetry of the molecule. The orientation of the

principal axis system relative to the field is then characterized by an elevation angle θ and an azimuth ϕ angle in of the perpendicular plane of the principal axes coordinates.

In isotropic solutions, the orientation dependence of the \mathbf{g} tensor is averaged by fast molecular motion and an isotropic g-value is observed:

$$\mathbf{g}_{\text{iso}} = \frac{1}{3}(\mathbf{g}_{\text{xx}} + \mathbf{g}_{\text{yy}} + \mathbf{g}_{\text{zz}}) \quad (\text{B.1.6})$$

The hyperfine interaction is one of the most important sources of information in EPR spectroscopy. It characterizes interactions between the electron spin and nuclear spins in its vicinity, thereby providing information about the direct magnetic environment of the spin. Its contribution to the Hamiltonian is given by:

$$\hat{H}_{\text{HF}} = \sum_{\mathbf{k}} \mathbf{S}^T \mathbf{A}_{\mathbf{k}} \mathbf{I}_{\mathbf{k}} = \hat{H}_{\text{iso}} + \hat{H}_{\text{aniso}} \quad (\text{B.1.7})$$

where \mathbf{A} is the hyperfine coupling tensor and $\mathbf{I}_{\mathbf{k}}$ is the spin operator of the \mathbf{k} -th coupled nucleus. This Hamiltonian can be further be subdivided into an isotropic contribution (\hat{H}_{iso}) and an anisotropic contribution (\hat{H}_{aniso}) contribution. The hyperfine coupling of the electron spin to a nuclear spin comes about by a through-space dipole-dipole coupling of the magnetic moments and is referred to as the Fermi contact interaction.

The Fermi contact interaction is due to the non-zero probability of finding the electron spin at some point in space where the nuclear spin also resides. This can only happen when the unpaired electron exists in an s-type orbital, because s-type orbitals are spatially symmetrical. Therefore the Fermi contact interaction leads to a purely isotropic contribution to the Hamiltonian:

$$\hat{H}_{\text{iso}} = \sum_{\mathbf{k}} a_{\text{iso}} \mathbf{S}^T \mathbf{I}_{\mathbf{k}} \quad (\text{B.1.8})$$

and a_{iso} can be expressed as:

$$a_{\text{iso}} = \rho_s \cdot \frac{2\mu_0}{3h} g_e \mu_B g_n \mu_n \langle \psi_0(\mathbf{0}) \rangle^2 \quad (\text{B.1.9})$$

ρ_s is the spin density in the s orbital of the k-th atom, and $\langle \psi_0(\mathbf{0}) \rangle^2$ is the probability of finding the electron at this nucleus in the ground state with wave-function ψ_0 . The magnetic moment on the electron is fully characterized by the g_e value of the free electron, as orbital angular momentum is non-existent in s-orbitals.

The anisotropic hyperfine coupling of the electron spin is a through-space dipole-dipole interaction. Unpaired electrons in -p, -d, and -f orbitals do not contribute to the Fermi contact interaction, because they have a node, which resides at the magnetic nucleus. However, due to the non-spherical symmetry of these orbitals, dipole-dipole couplings do not completely average. In a classical sense, the interaction between two magnetic dipoles $\boldsymbol{\mu}_1$ and $\boldsymbol{\mu}_2$ can be expressed as:

$$E = \frac{\mu_0}{4\pi r^3} [\boldsymbol{\mu}_1^T \boldsymbol{\mu}_2^T - \frac{3}{r^2} (\boldsymbol{\mu}_1^T \mathbf{r})(\boldsymbol{\mu}_2^T \mathbf{r})] \quad (\text{B.1.10})$$

where \mathbf{T} is the dipolar coupling tensor in the reference frame of the nucleus and r is the electron nuclear distance $r = (x^2 + y^2 + z^2)^{1/2}$. The anisotropic hyperfine interaction can be expressed in terms of the dipolar tensor by:

$$\hat{H}_{\text{aniso}} = \sum_k \mathbf{S}^T \mathbf{T}_k \mathbf{I}_k \quad (\text{B.1.11})$$

The hyperfine coupling tensor of a nucleus T_k , has matrix elements T_{ij} can be computed from the ground state wave function by:

$$T_{ij} = \frac{\mu_0}{4\pi} g_e \mu_B g_n \mu_n \langle \psi_0 | \frac{3r_i r_j - \delta_{ij} r^2}{r^5} | \psi_0 \rangle \quad (\text{B.1.12})$$

where $i, j = x, y, z$ and the angle brackets indicated that the electron is not localized on one point but is averaged over the electron spatial coordinates, and $\delta_{ij}=0$ or $\delta_{ii}=1$. The nine quantities T_{ij}

can therefore be arranged as a 3x3 matrix in the molecular reference frame ($i,j = x, y, z$) to yield the dipolar tensor:

$$\mathbf{T} = \begin{pmatrix} \mathbf{T}_{xx} & \mathbf{T}_{xy} & \mathbf{T}_{xz} \\ \mathbf{T}_{yx} & \mathbf{T}_{yy} & \mathbf{T}_{yz} \\ \mathbf{T}_{zx} & \mathbf{T}_{zy} & \mathbf{T}_{zz} \end{pmatrix} \quad (\text{B.1.13})$$

No matter what reference frame is chosen, the sum of the diagonal elements becomes zero because $r^2 = x^2 + y^2 + z^2$, so that the hyperfine tensor matrix is symmetrical about the diagonal. This implies that the off diagonal elements must take on a non-zero contribution; otherwise the diagonal would sum to zero. If this were the case the hyperfine tensor would only describe a spherical electron spin distribution about the magnetic nucleus. In solution, the fast molecular tumbling of the molecule cancels the orientation of the tensor and the only contribution to the hyperfine interaction is the isotropic condition.

The hyperfine coupling tensor can be computed in quantum chemistry programs such as Gaussian. Another method is to find a reference frame so that the off diagonal elements vanish and the trace reflects all the contributions of the spatial elements. The anisotropic hyperfine interaction is then a summation of contributions from the isotropic and anisotropic interactions. The general form of the anisotropic hyper interaction, without diagonalization is:

$$\mathbf{a}_{\text{aniso}} = \mathbf{a}_{\text{iso}} + \mathbf{T} \quad (\text{B.1.14})$$

The nuclear Zeeman interaction is analogous to the electron Zeeman interaction, only it is the nuclear spins which couple to the external magnetic field. This contribution is described by the nuclear Zeeman term:

$$\hat{\mathbf{H}}_{\text{NZ}} = \frac{-\mu_{\text{N}}}{\hbar} \sum_{\mathbf{k}} \mathbf{g}_{\text{n},\mathbf{k}} \mathbf{B}_0^{\text{T}} \mathbf{I}_{\mathbf{k}} \quad (\text{B.1.15})$$

The spin quantum number I and g_n factor are inherent properties of the k -th nucleus which carries a non-zero spin moment. In most cases, the nuclear Zeeman interaction can be considered isotropic as it hardly influences the CW-EPR spectra.

The structural features of paramagnetic molecules are in the hyperfine interactions with nuclei carrying spins. These interactions are detected in EPR by predictable splitting patterns in the signal, which arise from the spin multiplicities of the system. If the signal is overly broadened then these hyperfine interactions may be unresolved. The peak-to-peak line width (LW_{pp}) of the first derivative spectra is related to the full width at half maximum (FWHM) of the adsorption line:

$$\frac{LW_{pp}}{FWHM} = 3^{-1/2} \quad (B.1.16)$$

In angular frequency, the peak-to-peak line width is given by:

$$\Delta\omega_{pp} = \frac{2}{\sqrt{3}} T_2 \quad (B.1.17)$$

It can be estimated in terms of field units if unresolved hyperfine couplings do not significantly broaden the peaks, and the peaks retain an approximately Lorentzian shape:

$$\Delta B_{pp} = \frac{2}{\sqrt{3}} \frac{h}{T_2 g \mu_B} \quad (B.1.18)$$

In the cases where unresolved hyperfine couplings are present in the system, then the line shape may remain Lorentzian, it may broaden to become Gaussian shaped, or it can become a combination of Lorentzian and Gaussian. The latter case is known as a Voigtian line shape. In the extreme cases of Lorentzian broadening and both cases of Gaussian and Voigtian line broadening, equation x no longer becomes a good approximation of T_2 relation.

LITERATURE CITED

LITERATURE CITED

1. Alivisatos, A. P., Perspectives on the physical chemistry of semiconductor nanocrystals. *Journal of Physical Chemistry* **1996**, *100*, 13226-13239.
2. Nirmal, M.; Brus, L., Luminescence Photophysics in Semiconductor Nanocrystals. *Accounts of Chemical Research* **1998**, *32*, 407-414.
3. Zhao, J.; Bardecker, J. A.; Munro, A. M.; Liu, M. S.; Niu, Y.; Ding, I. K.; Luo, J.; Chen, B.; Jen, A. K.; Ginger, D. S., Efficient CdSe/CdS quantum dot light-emitting diodes using a thermally polymerized hole transport layer. *Nano Letters* **2006**, *6*, 463-467.
4. Peterson, M. D.; Cass, L. C.; Harris, R. D.; Edme, K.; Sung, K.; Weiss, E. A., The Role of Ligands in Determining the Exciton Relaxation Dynamics in Semiconductor Quantum Dots. *Annual Review of Physical Chemistry* **2014**, *65*, 317-339.
5. Murray, C. B.; Norris, D. J.; Bawendi, M. G., Synthesis and characterization of nearly monodisperse CdE (E = sulfur, selenium, tellurium) semiconductor nanocrystallites. *Journal of the American Chemical Society* **1993**, *115*, 8706-8715.
6. Yin, Y.; Alivisatos, A. P., Colloidal nanocrystal synthesis and the organic-inorganic interface. *Nature* **2005**, *437* (7059), 664-670.
7. Frederick, M. T.; Amin, V. A.; Weiss, E. A., Optical Properties of Strongly Coupled Quantum Dot–Ligand Systems. *The Journal of Physical Chemistry Letters* **2013**, *4*, 634-640.
8. Munro, A. M. Selenide and Sulfide Quantum Dots and Nanocrystals: Optical Properties. In *Handbook of Luminescent Semiconductor Materials*, CRC Press: Boca Rotan, Florida, 2011; pp 307-320.
9. Nose, K.; Fujita, H.; Omata, T.; Otsuka-Yao-Matsuo, S.; Nakamura, H.; Maeda, H. Chemical Role of Amines in the Colloidal Synthesis of CdSe Quantum Dots and Their Luminescence Properties. *Journal of Luminescence*. **2007**, *126*, 21-26.
10. Klimov, V. I.; McBranch, D. W.; Leatherdale, C. A.; Bawendi, M. G., Electron and hole relaxation pathways in semiconductor quantum dots. *Physical Review B* **1999**, *60*, 13740-13749.
11. Dabbousi, B. O.; Rodriguez-Viejo, J.; Mikulec, F. V.; Heine, J. R.; Mattoussi, H.; Ober, R.; Jensen, K. F.; Bawendi, M. G., (CdSe)ZnS Core–Shell Quantum Dots: Synthesis and Characterization of a Size Series of Highly Luminescent Nanocrystallites. *The Journal of Physical Chemistry B* **1997**, *101*, 9463-9475.

12. Kuno, M. L., J. K.; Dabbousi, B. O.; Mikulec, F. V.; Bawendi, M.G., The band edge luminescence of surface modified CdSe nanocrystallites: Probing the luminescing state. *The Journal of Physical Chemistry* **1997**, *106*, 9869-9889.
13. Talapin, D. V.; Rogach, A. L.; Kornowski, A.; Haase, M.; Weller, H., Highly Luminescent Monodisperse CdSe and CdSe/ZnS Nanocrystals Synthesized in a Hexadecylamine–Trioctylphosphine Oxide–Trioctylphosphine Mixture. *Nano Letters* **2001**, *1*, 207-211.
14. Landes, C.; Burda, C.; Braun, M.; El-Sayed, M. A., Photoluminescence of CdSe Nanoparticles in the Presence of a Hole Acceptor: n-Butylamine. *Jouranal of Physical Chemistry B* **2001**, *105*, 2981-2986.
15. Ji, X.; Copenhaver, D.; Sichmeller, C.; Peng, X., Lignad bonding dynamics on colloidal nanocrystals at room temperature: The case of alkylamines on CdSe nanocrystals. *Journal of American Chemical Society* **2008**, *130*, 5726-5735.
16. Kalyuzhny, G.; Murray, R. W., Ligand Effects on Optical Properties of CdSe Nanocrystals. *Journal of Physical Chemistry B* **2005**, *109*, 7012-7021.
17. Munro, A. M.; Jen-La Plante, I.; Ng, M. S.; Ginger, D. S., Quantitative Study of the Effects of Surface Ligand Concentration on CdSe Nanocrystal Photoluminescence. *The Journal of Physical Chemistry C* **2007**, *111*, 6220-6227.
18. Knowles, K. E.; Tice, D. B.; McArthur, E. A.; Solomon, G. C.; Weiss, E. A., Chemical control of the photoluminescence of CdSe quantum dot-organic complexes with a series of para-substituted aniline ligands. *Journal of the American Chemical Society* **2010**, *132*, 1041-1050.
19. Omogo, B.; Aldana, J. F.; Heyes, C. D., Radiative and Nonradiative Lifetime Engineering of Quantum Dots in Multiple Solvents by Surface Atom Stoichiometry and Ligands. *The Journal of Physical Chemistry C* **2013**, *117*, 2317-2327.
20. Fischer, S. A.; Crotty, A. M.; Kilina, S. V.; Ivanov, S. A.; Tretiak, S., Passivating ligand and solvent contributions to the electronic properties of semiconductor nanocrystals. *Nanoscale* **2012**, *4*, 904-914.
21. Munro, A. M.; Plante, I. J.-L.; Ng, M. S.; Ginger, D. S., Quantitative Study of the Effects of Surface Ligand Concentration on CdSe Nanocrystal Photoluminescence. *Journal of Physical Chemistry C* **2007**, *111*, 6220-6227.
22. Munro, A. M.; Ginger, D. S., Photoluminescence Quenching of Single CdSe Nanocrystals by Ligand Adsorption. *Nano Letters* **2008**, *8*, 2585-2590.
23. Jeong, S.; Achermann, M.; Nanda, J.; Ivanov, S.; Klimov, V. I.; Hollingsworth, J. A., Effect of the Thiol-Thiolate Equilibrium on the Photophysical Properties of Aqueous CdSe/ZnS Nanocrystal Quantum Dots. *Journal of the American Chemical Society* **2005**, *127*, 10126-10127.

24. Wuister, S. F.; Swart, I.; van Driel, F.; Hickey, S. G.; de Mello Donegá, C., Highly Luminescent Water-Soluble CdTe Quantum Dots. *Nano Letters* **2003**, *3*, 503-507.
25. Wang, F.; Tang, R.; Buhro, W. E., The Trouble with TOPO; Identification of Adventitious Impurities Beneficial to the Growth of Cadmium Selenide Quantum Dots, Rods, and Wires. *Nano Letters* **2008**, *8*, 3521-3524.
26. Becerra, L. R.; Murray, C. B.; Griffin, R. G.; Bawendi, M. G., Investigation of the surface morphology of capped CdSe nanocrystallites by ^{31}P nuclear magnetic resonance. *Journal Chemical Physics* **1994**, *100*, 3297-3300.
27. Evans, C. M.; Evans, M. E.; Krauss, T. D., Mysteries of TOPSe Revealed: Insights into Quantum Dot Nucleation. *Journal of the American Chemical Society* **2010**, *132*, 10973-10975.
28. Kopping, J. T.; Patten, T. E., Identification of acidic phosphorus-containing ligands involved in the surface chemistry of CdSe nanoparticles prepared in tri-N-octylphosphine oxide solvents. *Journal of the American Chemical Society* **2008**, *130*, 5689-5698.
29. Aldana, J.; Wang, Y. A.; Peng, X., Photochemical Instability of CdSe Nanocrystals Coated by Hydrophilic Thiols. *Journal of the American Chemical Society* **2001**, *123*, 8844-8850.
30. Aldana, J.; Lavelle, N.; Wang, Y.; Peng, X., Size-Dependent Dissociation pH of Thiolate Ligands from Cadmium Chalcogenide Nanocrystals. *Journal of the American Chemical Society* **2005**, *127*, 2496-2504.
31. Oosterkamp, T. H.; Fujisawa, T.; van der Wiel, W. G.; Ishibashi, K.; Hijman, R. V.; Tarucha, S.; Kouwenhoven, L. P., *Nature* **1998**, *395*, 873-878.
32. Hassinen, A.; Moreels, I.; de Mello Donega, C.; Martins, J. C.; Hens, Z., Nuclear Magnetic Resonance Spectroscopy Demonstrating Dynamic Stabilization of CdSe Quantum Dots by Alkylamines. *Journal of Physical Chemistry Letters* **2010**, *1*, 2577-2581.
33. Gomes, R.; Hassinen, A.; Szczygiel, A.; Zhao, Q.; Vantomme, A.; Martins, J. C.; Hens, Z., Binding of Phosphonic Acids to CdSe Quantum Dots: A Solution NMR Study. *J. Journal of Physical Chemistry Letters* **2011**, *2*, 145-152.
34. Milliron, D. J.; Alivisatos, A. P.; Pitois, C.; Edder, C.; Frechet, J. M. J., Electroactive surfactant designed to mediate electron transfer between CdSe nanocrystals and organic semiconductors. *Advanced Materials* **2003**, *15*, 58-61.
35. Morris-Cohen, A. J.; Malicki, M.; Peterson, M. D.; Slavin, J. W. J.; Weiss, E. A., Chemical, Structural, and Quantitative Analysis of the Ligand Shells of Colloidal Quantum Dots. *Chemistry of Materials*. **2013**, *25*, 1155-1165.

36. Sachleben, J. R.; Colvin, V.; Emsley, L.; Wooten, E. W.; Alivisatos, A. P., Solution-State NMR Studies of the Surface Structure and Dynamics of Semiconductor Nanocrystals. *Journal of Physical Chemistry B* **1998**, *102*, 10117-10128.
37. Eaton, S. S.; Eaton, G. R., The world as viewed by and with unpaired electrons. *Journal of Magnetic Resonance* **2012**, *223*, 151-163.
38. Boocock, D. G. B.; Darcy, R.; Ullman, E. F., Studies of Free Radicals. II. Chemical Properties of Nitronyl Nitroxides. A Unique Radical Anion. *Journal of the American Chemical Society* **1968**, *90*, 5945-5946.
39. Ullman, E. F.; Osiecki, J. H.; Boocock, D. G. B.; Darcy, R., Studies of Stable Free Radicals. X. Nitronyl Nitroxide Monoradicals and Biradicals as Possible Small Molecule Spin Labels. *Journal of the American Chemical Society* **1972**, *94*, 7049-7059.
40. Caneschi, A.; Gatteschi, D.; Rey, P., The Chemistry and Magnetic Properties of Metal Nitronyl Nitroxide Complexes. In *Progress in Inorganic Chemistry, Volume 29*, John Wiley & Sons, Inc., Hoboken, New Jersey, 1991; pp 331-429.
41. Beaulac, R.; Bussiere, G.; Reber, C.; Lescop, C.; Luneau, D., Solid-state absorption and luminescence spectroscopy of nitronyl nitroxide radicals. *New Journal of Chemistry* **2003**, *27*, 1200-1206.
42. Beaulac, R.; Luneau, D.; Reber, C., The emitting state of the imino nitroxide radical. *Chemical Physics Letters* **2005**, *405*, 153-158.
43. Zheludev, A.; Barone, V.; Bonnet, M.; Delley, B.; Grand, A.; Ressouche, E.; Rey, P.; Subra, R.; Schweizer, J., Spin density in a nitronyl nitroxide free radical. Polarized neutron diffraction investigation and ab initio calculations. *Journal of the American Chemical Society* **1994**, *116*, 2019-2027.
44. McConnell, H. M., Electron Densities in Semiquinones by Paramagnetic Resonance. *The Journal of Chemical Physics* **1956**, *24*, 632-632.
45. Karplus, M.; Fraenkel, G. K., Theoretical Interpretation of Carbon - 13 Hyperfine Interactions in Electron Spin Resonance Spectra. *The Journal of Chemical Physics* **1961**, *35*, 1312-1323.
46. Zheludev, A.; Bonnet, M.; Luneau, D.; Ressouche, E.; Rey, P.; Schweizer, J., The spin density in an imino nitroxide free radical: A polarized-neutron study. *Physica B: Condensed Matter* **1995**, *213-214*, 268-271.
47. Zheludev, A.; Bonnet, M.; Delley, B.; Grand, A.; Luneau, D.; Örstöm, L.; Ressouche, E.; Rey, P.; Schweizer, J., An imino nitroxide free radical: Experimental and theoretical spin density and electronic structure. *Journal of Magnetism and Magnetic Materials* **1995**, *145*, 293-305.

48. Helbert, J. N.; Kopf, P. W.; Poindexter, E. H.; Wagner, B. E., Complexing and protonation of free-radical imidazolin-1-oxyl and imidazolin-1-oxyl 3-oxide ligands: a magnetic-resonance investigation. *Journal of the Chemical Society, Dalton Transactions* **1975**, 11, 998-1006.
49. Eaton, S. S.; Eaton, G. R., Interaction of spin labels with transition metals. *Coordination Chemistry Reviews* **1978**, 26, 207-262.
50. Hoffman, B. M.; Eames, T. B., Free-radical molecular complexes. *Journal of the American Chemical Society* **1969**, 91, 5168-5170.
51. Hoffman, B. M.; Eames, T. B., Protonated nitroxide free radical. *Journal of the American Chemical Society* **1969**, 91, 2169-2170.
52. Ressouche, E.; Boucherle, J. X.; Gillon, B.; Rey, P.; Schweizer, J., Spin density maps in nitroxide-copper(II) complexes. A polarized neutron diffraction determination. *Journal of the American Chemical Society* **1993**, 115, 3610-3617.

Chapter 2

Synthesis and Characterization

2.1 General Considerations

This chapter describes the synthesis of CdTe QDs and nitronyl and imino nitroxide radicals. CdTe were characterized using UV-VIS spectroscopy. All adsorption spectra were collected on an OLIS17 UV/VIS/NIR spectrophotometer obtained in 1nm/s increments. The UV-VIS spectra of CdTe were taken in distilled toluene (over sodium metal/diphenylketyl anion) in a quartz cuvette with a length of 1 cm.

The precursors to both radicals were characterized with a combination of ^1H NMR and melting point analysis. The NMR instrument used was an Agilent DDR2 500 MHz NMR spectrometer equipped with a 7600AS autosampler. Samples were submitted to the instrument in a quartz tube. Melting points were measured on a Mel-Temp II apparatus equipped with a mercury thermometer. The average temperature increase for melting point analysis was kept to approximately 2°C per minute. The melting points were then compared to known values where available. The infrared spectra of both radicals were recorded on a Mattson Galaxy 3025, after being mixed with dried KBr and crushed into a solid pellet. Elemental analyses of each radical were obtained at third party facility at Michigan State University. The mass spectrum of nitronyl nitroxide was also obtained from a third party facility, The Mass Spectrometry Core of the Research Technology Support Facility at Michigan State University. Samples were submitted in acetonitrile (dried over $\sim 3\text{\AA}$ molecular sieves) for high-resolution mass spectrometry analysis.

2.2 CdTe Quantum Dot Synthesis and Characterization

All CdTe QDs (~3-4 nm) were prepared from a procedure adapted from Peng and Peng.¹ All reagents, trioctylphosphine oxide (TOPO, 98%), trioctylphosphine (TOP, 97%), tellerium powder (200 mesh, 99.99%), hexadecylamine (HDA), and cadmium oxide (99.99%) were used as received from Aldrich. The general procedure is as follows: Trioctylphosphine oxide (10 mL), HDA (200 μ L), and cadmium oxide (0.0256 g, 0.20 mmol) were added to a dry 50-mL three neck round bottom flask, which was heated to approximately 320 °C with stirring under positive nitrogen flow. After a sufficient time has passed (~2 hr) the reaction mixture should appear clear and the solvent should be adequately purged of oxygen. At this point, a previously prepared solution of trioctylphosphine telluride solution (TOP-Te, 0.20 mmol) is injected which causes a rapid decrease in temperature to induce crystallization. The resultant red solution is kept at a temperature of approximately 280 °C for twenty minutes, at which point the heating element is removed and the solution was allowed to cool to room temperature. After sufficient cooling, 10 mL of toluene or hexanes is injected into the reaction mixture. A white precipitate is allowed to form, which is comprised of excess cadmium oxide, TOPO, and HDA. This precipitate is removed from the red supernatant by centrifugation (at 2700 rpm for 10 min) and discarded. The addition of methanol (~2:1 v/v) induces the precipitation of the QDs, which are removed from the supernatant with further ^{centrifugation}. The resultant clear supernatant can then be discarded as it is now composed of mostly HDA and TOPO. The quantum dots were then stored until further use.

The relative dispersion of the CdTe nanocrystal diameters were determined by fitting the first excitonic peak maxima (λ) to the following analytical equation as detailed by Peng:¹

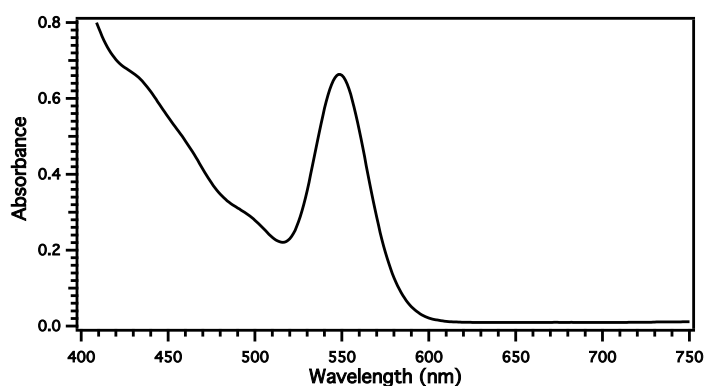
$$D = (9.8127 \times 10^{-7})\lambda^3 - (1.7147 \times 10^{-3})\lambda^2 + 1.0064\lambda - 194.84 \quad (2.2.1)$$

where D is the diameter of the CdTe nanocrystal and λ corresponds to the first excitonic peak as measured in solution. This can then be used to calculate the molar extinction coefficient ϵ of the sample:

$$\epsilon = 10043(D)^{2.12} \quad (2.2.2)$$

A representative adsorption spectra of a 3.2nm CdTe sample (concentration = 5.80 μM) is shown below in figure 2.1.

Figure 2.1. The adsorption profile of the first excitonic peak used to calculate the relative sample diameter and concentration of a CdTe sample. ($D = 3.2 \text{ nm}$, concentration = 5.80 μM)



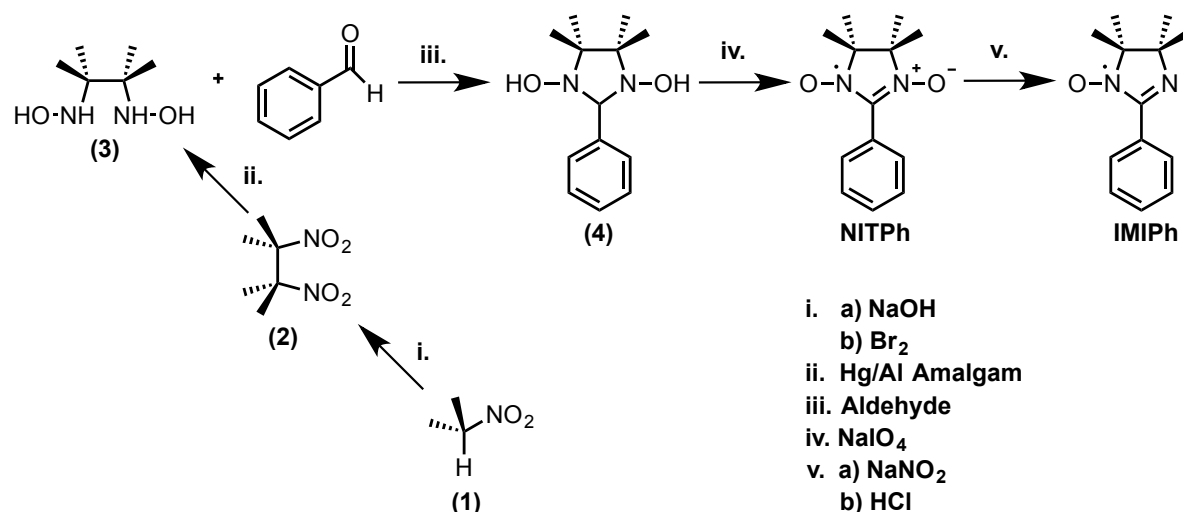
The width of the peak is indicative of the size distribution of the sample. To take these varying size distributions into account in calculating the samples overall concentration, the adsorption should be read from the half width half maximum value.

2.3 Synthesis of NITPh and IMIPh:

Both the NIT-Phenyl nitroxide and IMI-Phenyl nitroxide were prepared by following a slight modification of the literature.² The reaction scheme is outlined in Scheme 2.1. The primary difference in this work is the synthetic approach of 2,3-Bis(hydroxyamino)-2,3-dimethylbutane precursor (3). 2-nitropropane (1) and Benzaldehyde were purchased from Aldrich and used without further purification.

(1) ¹H NMR (500 MHz, CDCl₃): δ = 1.13 (s, CH₃)

Scheme 2.1. The general reaction scheme of NITPh and IMIPh.



2,3-dimethyl-2,3-dinitrobutane (2)

85 mL of a 6 M sodium hydroxide solution is added to a 2 L round bottom flask, which is then cooled in an ice bath with rapid stirring. 45 ml (0.5 mol) of 2-nitropropane is then added slowly via drop wise addition so that the solution temperature is maintained below 5° C. With continued stirring 14 mL (0.27 mol) of bromine is added via slow drop wise addition so that the reaction mixture is maintained below 5° C. After the final addition the solution is maintained on an ice bath for about an hour, at which point it is removed from the ice bath and allowed to return to room temperature. 160 mL of ethanol is then added to the reaction mixture, and the

mixture is then refluxed for 3 hours. The solution should turn from a light yellow to a dull orange, and then finally a white precipitate should begin to appear which out to form a slurry in solution. After 3 hours the heating is stopped. When the solution returns to room temperature, 250 g of crushed ice and 250 mL of ice cold water is added to the solution to induce the precipitation of a white product (**2**). This product is then collected on a sintered funnel under vacuum and dried in a vacuum desiccator for 2 days. 2,3-dimethyl-2,3-dinitrobutane (**2**) is recrystallized from hot methanol with 10mL of solvent per 1 gram of crude dry solid. After 1 night in the refrigerator, ~30 g of a white crystalline flask of (**2**) is collected.

Yield = 62%

m.p. - 212° C

¹H NMR (500 MHz, CDCl₃): δ = 1.11 (s, CH₃) δ = 1.32 (s, NH₂)

2,3-Bis(hydroxyamino)-2,3-dimethylbutane (3)

9.3 g (0.09 mol) of pure aluminum foil is ripped into small pieces, added to a 500 mL Erlenmeyer flask, and covered with enough water to submerge all of the pieces. In a separate 250 mL beaker, 9.3 g (0.03 mol) of finely powered mercury chloride is thoroughly dissolved in 60 mL of water. The mercury chloride solution is then added to the aluminum pieces and is stirred for 4 minutes. The resulting amalgam is washed twice with water, followed by ethanol, and then with 3 aliquots of THF. The amalgam is then submerged with THF in a 1 L round bottom flask. This is then placed in an ice bath under strong magnetic stirring. In a separate flask, 6.24g (0.03 mol) of 2,3-dimethyl-2,3-dinitrobutane is dissolved in 20 mL of THF. The 2,3-dimethyl-2,3-dinitrobutane solution is then added to the cooled amalgam, along with 8.4 mL of chilled water. This is allowed to react for 45 minutes at which point the reaction is washed down a silica plug with three excess washings of THF. The reaction is washed further with three 60

mL portions of methanol. The solvent is then removed under vacuum yielding ~2.20g of a fine white crystalline powder (**3**), which is then washed with DCM.

Yield = 62%

m.p. = 182° C

¹H NMR (500 MHz, D₂O): δ = 1.27 (s, CH₃)

1,3-Dihydroxy-2-phenyl-4,4,5,5-tetramethylimidazolines (4)

1.85 g of Benzaldehyde (0.017 mol) is dissolved in 10 mL of diethyl ether which is added by slow drop wise addition to a ice cooled solution of 2,3-diamino-2,3-dimethylbutane (**3**) (2g, 0.017 mol) which is dissolved 20 mL THF. The reaction vessel was then transferred to a refrigerator (0° C) and left overnight to complete the condensation reaction. The solution was then evaporated under vacuum at low temperature to yield a white crystalline powder. The crude product (**4**) was then collected without further purification or characterization.

NITPh

2 g of crude 1,3-Dihydroxy-2-phenyl-4,4,5,5-tetramethylimidazolines (0.01 mol) is dissolved in 100 mL of methylene chloride and placed in an ice bath under constant stirring. A solution of NaIO₄ (3.1g, 0.02 mol) in 50 mL of water is then added to the chilled solution at a slow rate so that the temperature of the reaction flask does not exceed 5° C. The solution gradually develops a deep blue hue, which is characteristic of nitronyl nitroxide radicals. The reaction was followed by TLC (SiO₂, 50% ethyl acetate/50% hexanes v/v) and allowed to go until completion. After the reaction is completed the solvent is evaporated rapidly under vacuum, the crude product is then collected and purified by chromatography (SiO₂, 40% ethyl acetate/60%hexanes v/v). Deep blue crystals formed upon refrigeration (0° C) and could be recrystallized by slow evaporation of ether at low temperatures (0° C).

Yield = 53%

Elemental Analysis:

Calculated (%) for $C_{13}H_{17}N_2O_2$: C (66.9%), H(7.35%), N(12.01%)

Found: C (66.50%), H(7.49%), N(11.56%)

IR (KBr): 1394 cm^{-1} (ν_{N-O}), 1368 cm^{-1} (ν_{N-O})

ESI-MS (m/e):

Calculated: 234.1361 [M^+]

Found: 234.1368 [M^+]

IMIPh

1g of NITPh (4.3 mmol) is dissolved in 150 mL of dichloromethane and placed in an ice bath under constant stirring. A solution of sodium nitrite (1.2g, 17.2 mmol) in 100 mL of water is added to the reaction mixture all at once. Hydrochloric acid (0.25M) is then added to this solution by dropwise addition. The solution gradually changes from a deep blue to a red/orange color indicating the formation of the imino nitroxide radical. The addition of hydrochloric acid is stopped when the nitroxide precursor can no longer be detected by TLC (SiO_2 , 50% ethyl acetate/50% hexanes v/v). After the reaction is completed the solvent is evaporated rapidly under vacuum. The crude product is then collected and purified by chromatography (SiO_2 , 40% ethyl acetate/60%hexanes v/v). The final product is collected as a viscous and deeply colored orange liquid. A deep orange colored crystal could be induced by the slow evaporation of the liquid in a refrigerator. This crystal quickly reverted back into a viscous liquid at room temperature.

Yield = 63%

Elemental Analysis:

Calculated (%) for C₁₃H₁₇N₂O₂ : C (71.86%), H(7.89%), N(12.89%)

Found: C (71.63%), H(8.03%), N(13.06%)

IR (KBr): 1364 cm⁻¹ (ν_{N-O})

2.4 Conclusions

The general synthesis and characterization of CdTe QDs is described. In addition the synthesis of nitronyl and imino nitroxide radicals is also detailed. This procedure is slightly modified from that reported in literature, namely mercury aluminum amalgam was used as the reducing agent of the bis-hydroxylamine precursor. The characterization of both radicals and their precursors was performed with a combination ¹H NMR spectroscopy, melting point analysis, elemental analysis, IR spectroscopy, and high-resolution mass spectrometry.

LITERATURE CITED

LITERATURE CITED

1. Yu, W. W.; Qu, L.; Guo, W.; Peng, X., Experimental Determination of the Extinction Coefficient of CdTe, CdSe, and CdS Nanocrystals. *Chemistry of Materials* **2003**, *15*, 2854-2860.
2. Hirel, C.; Vostrikova, K. E.; Pécaut, J.; Ovcharenko, V. I.; Rey, P., Nitronyl and Imino Nitroxides: Improvement of Ullman's Procedure and Report on a New Efficient Synthetic Route. *Chemistry – A European Journal* **2001**, *7*, 2007-2014.

Chapter 3

EPR Spectroscopy of NITPh/IMIPh and CdTe QDs

3.1 Introduction

In the previous chapter (Chapter 1.7), the use of EPR spectroscopy in conjunction with nitronyl and imino nitroxide radicals acting as spin probe ligands for studying the coordination chemistry of a variety of metal ions was briefly introduced. The same concept may also offer insight into the binding interactions of NITPh and IMIPh radicals after their introduction as ligands into a CdTe QD system. Using EPR spectroscopy may also alleviate some of the limitations encountered with NMR spectroscopy and could further aid studies relying on fluorescence spectroscopy.

Specifically, EPR spectroscopy can eliminate the noise associated with NMR spectroscopy, by targeting only the radical ligand. Therefore the only chemical changes observed in the system will be that of the radical. These changes include any associated reactions that may occur to the radical ligands as a result of surface binding or any chemical interactions with the CdTe QDs native ligands.

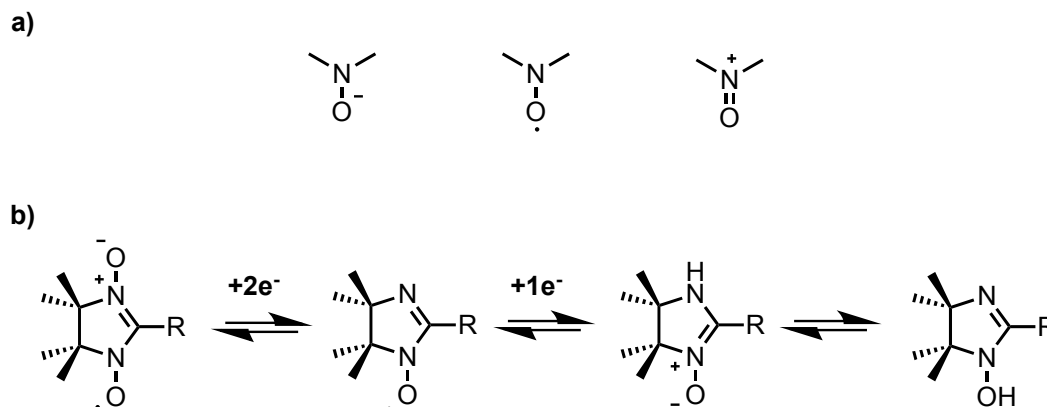
If coordination occurs, it is expected that both nitronyl and imino nitroxide radicals will donate their valence electrons to the Cd^{2+} surface ions, given that both radicals behave as Lewis-bases. If both ligands retain their radical nature upon coordination, then direct experimental evidence of surface binding would be observed in the appearance of Cd^{2+} hyperfine structures, which are known as satellite features. As two isotopes of cadmium are spin active species, ^{111}Cd ($I = 1/2$) and ^{113}Cd ($I = 1/2$), Cd^{2+} satellite features due to nitroxide radical coordination can exist as a result of spin polarization from the nitroxide nitrogen or the imine nitrogen onto the metal center.¹

In the case of NITPh, these satellite features are expected to be very weak, as spins on the metal center must be polarized from the spin density on the nitroxide nitrogen and over the multiple bonds on the oxygen. On the other hand, the existence of satellite features for the IMIPh radical may be stronger due to decreased bond distance from the imine nitrogen to the metal center.

In addition to any observable satellite features of the metal, the hyperfine coupling constants of both the nitroxide nitrogen and the imine nitrogen are expected to increase proportionately to their surface donor strength. As surface coordination involves the redistribution of spin density to the p_z orbitals of the nitroxide nitrogen or the imine nitrogen, most of the observable changes in the hyperfine interaction will occur in anisotropic spectra. The results of this thesis only examine the isotropic spectra of both radicals before and after they are introduced into the CdTe QD system.

In addition to detecting any surface binding, EPR spectroscopy should be able to monitor any reactions the radicals may undergo with either the surface of the CdTe QDs or its surrounding ligands. While nitroxide radicals are generally regarded as being chemically stable, in some cases they have been known to participate in redox chemistry. In general the nitroxide bond is the active site for redox chemistry. The oxidation state of nitroxide radicals can be considered as existing at an intermediate between the hydroxylamino anion and a nitrosonium cation as shown in figure 3.1a. Salts of the nitrosonium cations have been obtained from $\text{Cu(II)} \cdot \text{ClO}_4$,² Sn(IV) halides³, and $\text{Pd(II)Cl(PPh}_3)_3$.⁴ In addition to this, nitroxide radicals are also known to be labile to oxidation with molecular chlorine, bromine, triphenylmethylcarbonium salts, and oxygen in the presence of silver oxide.^{5,6}

Figure 3.1. a) The hydroxylamino anion, nitroxide radical, and nitrosonium cation groups b) A two-electron reduction of nitronyl nitroxide yields imino nitroxide. A three electron reduction results in two tautomers: amidino and the hydroxlamino which are in equilibrium.



In most cases, a proton source is required to reduce a nitroxide to a hydroxylamine. The reduction reactions of nitroxide radicals in acidic media occurs with elementary alkali metals, zinc, tin, iodine, and hydrogen in the presence of platinum.⁷ The reduction of Nitronyl nitroxides to imino nitroxides was found to occur with Mn(II)(hfac)₂ in refluxing heptanes.⁸ Although imino nitroxide was found to be the more likely reduced species, two other reduced forms existed in tautomeric equilibrium, the amidino derivative and the hydroxlamino derivative, as shown in figure 3.1b. The reduction of nitronyl nitroxide was attributed to a two-electron process, while an additional electron transfer was responsible for its two further reduced tautomeric forms.

In addition to participating in redox chemistry with a variety of metals, nitronyl nitroxides are reduced to imino nitroxides in the presence of triphenylphosphine. This reaction was found to occur at refluxing temperatures and even occurred in non-polar solvents such as benzene.⁹ This is significant as phosphine ligands; specifically trioctylphosphine are commonly present during and after the synthesis of CdTe QDs.

3.2 Experimental

Mixtures of CdTe/NITPh and CdTe/IMIPh. The CdTe QDs used were synthesized and characterized as discussed in in the previous chapter (chapter 2.2). The diameters of each QD was kept as consistently as possible between the ranges of 3.4 - 3.6 nm as determined by UV-VIS Spectroscopy. The native ligands used for these samples were trioctylphosphine and trioctylphosphine oxide. Both radicals, NITPh and IMIPh were mixed with the QD solutions at two different ratios, 100 μM Radical/1 μM CdTe QD and 200 μM Radical/1 μM CdTe. After mixing, an ~ 0.4 mL aliquot was transferred to high-grade quartz EPR tube with a diameter of 7 mm and a length of 144 mm. After transferring the aliquot, the EPR tube was immediately fixed with airtight septa. This mixture was then subjected to three freeze pump thaw cycles in liquid nitrogen under nitrogen gas to remove excess air. Because triphenylphosphine is a known reducing agent of NITPh under some chemical conditions, as a control, a mixture of trioctylphosphine and NITPh (1:1 at 100 μM) was also tested with CW-EPR spectroscopy. The samples were performed in toluene, and were subjected to three freeze pump thaw cycles before measurement.

CW-EPR. The CW-EPR spectrums of the Radical/CdTe QD mixtures were then recorded over an extended period of time, in approximately 30-minute intervals. The EPR instrument used in all of the studies was a Bruker ESP-300E CW-EPR spectrometer, which operates at an X-band frequency. A Bruker TE-102 cavity probe connected to an external microwave counter was used to accurately assess the frequency of the probe. The probe was tuned to the solution containing the pure radical prior to measuring the radical/CdTe QD mixture. The concentrations of the pure solution of both radicals were maintained at the same concentration of the CdTe/radical mixture. The solution containing the pure radical was also subjected to the same

freeze pump thaw cycles as the mixture, and the same quartz EPR tube used to measure the spectra of the pure radical was also used for the radical/CdTe QD mixture.

Ligand Exchange. Octadecylamine (97%) was purchased from Sigma-Aldrich and used without further purification for the ligand exchange procedures. To remove the native phosphine ligands, namely trioctylphosphine and trioctylphosphine oxide from the 3.6 nm CdTe QDs, octadecylamine was added in excess. After addition, the solution was allowed to equilibrate for 10 min, at which point the CdTe QDs were crashed out of solution by the addition of methanol. The CdTe QDs were then separated and concentrated as a supernatant by centrifugation (~3,500 rpm). After the supernatant was collected the CdTe QDs containing the new ligands were re-suspended in toluene. This procedure was repeated until satisfactory removal of all of the native phosphine ligands TOP and TOPO had been completed. This was achieved by the following the disappearance of ^{31}P peak using NMR spectroscopy. The results of the ^{31}P NMR prior to and following the ligand exchange procedure are shown in the appendix at the end of this chapter. Also shown in this appendix are the result absorbance spectra of CdTe prior too and following the ligand exchange procedure.

CW-EPR Data Analysis. The energy eigenvalues for both nitronyl and imino nitroxide radicals are determined through the solution of the Schrödinger equation. For the fast tumbling radical the CW-EPR spectra can be considered isotropic, and the eigenstates obtained have energies (E):

$$E = g_{\text{iso}}\mu_B B_0 m_s - g_n\mu_n B_0 m_I + a_{\text{iso}} m_s m_I \quad (3.2.1)$$

The selection rules for CW-EPR transitions are $\Delta m_s = \pm 1$ and $\Delta m_I = 0$. The theoretical number of observed transitions in the CW-EPR spectrum is referred to as the spin multiplicity (n):

$$n = \prod_i (2k_i I_i + 1) \quad (3.2.2)$$

In equation the index i runs over the groups of equivalent nuclei, k_i are the numbers of nuclei within each group, and I_i are their nuclear spin quantum numbers.

The number of transition frequencies expected for nitronyl nitroxide radicals ($i, k = 2$; $I=1$) is 5, with a intensity ratio pattern of 1:2:3:2:1. The number of transitions expected for imino nitroxide radicals ($i = 2$; $k=1,2$; $I=1$) is 9, with a intensity splitting pattern of 1:1:1:1:1:1:1:1:1. For most spectra the nuclear Zeeman interaction is considered negligible, so that the allowed EPR transitions occur at frequencies:

$$\Delta E = h\nu = g_{\text{iso}}\mu_B B_0 + a_{\text{iso}} m_I \quad (3.2.3)$$

and are due solely to the electron Zeeman and the hyperfine interaction. Regarding imino nitroxide, while 9 distincts eigenstates are obtained from the spin Hamiltonian typically only 7 transitions are observed. This is due to an accidentally degeneracy between two hyperfine couplings energies. This degeneracy is common in radicals where the value of one hyperfine constant is approximately half the energy of the other and it usually leads to a splitting pattern of 1:1:2:1:2:1:1. For each of the pure radical solutions, the peak-to-peak line widths in field units were used to estimate the spin-spin relaxation times (T_2) of the radicals using:

$$\Delta B_{\text{pp}} = \frac{2}{\sqrt{3}T_2} \frac{h}{g\mu_B} \quad (3.2.4)$$

To accurately assess the CW-EPR signal intensity of the radicals and any subsequent changes that might occur as a result mixing, the signal intensity of each spectrum was normalized to 1. The total area of the signal is defined as second integration of the total signal intensity and it is proportional to the total population of radicals in the mixture. A cumulative trapezoidal integration model was used to calculate the total signal intensity. This value was

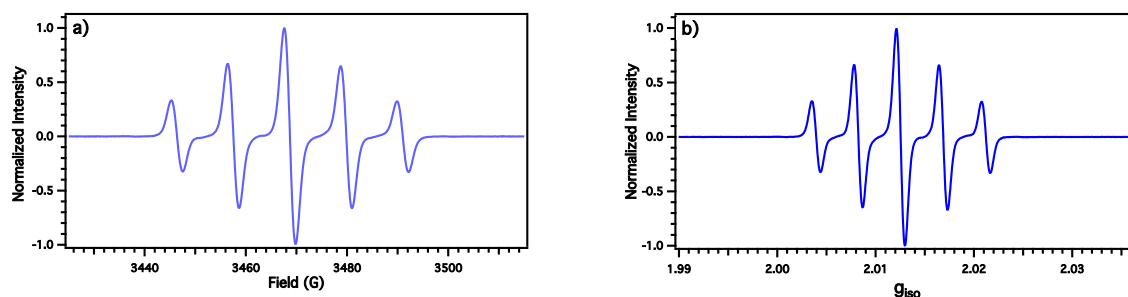
then normalized to the largest integrated area at each time point. The total signal intensity of the pure radical solution was also normalized to 1, using the largest integrate area post mixing.

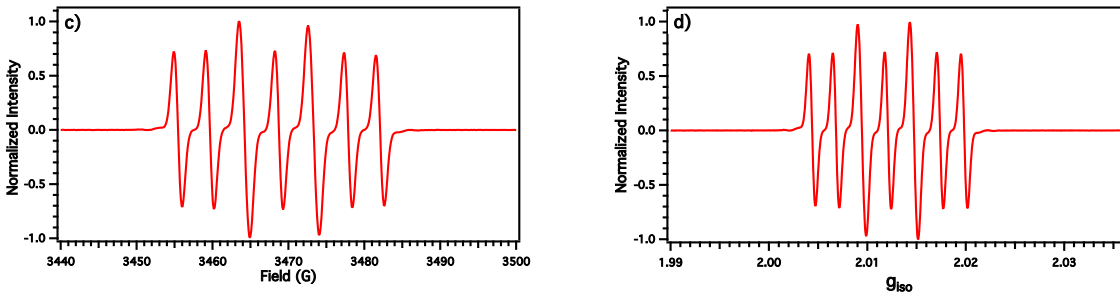
3.3 Results and Discussion

Isotropic CW-EPR - NITPh and IMIPh. The CW-EPR spectra of 100 μM NITPh is shown in figure 3.2a. The hyperfine splitting pattern is an expected quintet, with an isotropic value of $a_n = 7.3$ G, which is in agreement with previous results.¹⁰ The measured isotropic g-value is shown in figure 3.2b with a measured g_{iso} value of 2.012. The line shape is best described as Lorentzian with a width (lwpp) of $\Delta B = 2.23$ G as measured from the highest-field line. This gives an approximate spin-spin relaxation value of $T_2 = 2.94 \times 10^{-8}$ s assuming the absence of any unresolved couplings contributing to the line width.

The CW-EPR spectra of 100 μM IMIPh is shown in figure 3.2c. The hyperfine splitting pattern is an expected 7-line splitting pattern, with the isotropic splitting values of $a_{n1} = 4.19$ G and $a_{n2} = 9.07$ G, which is also in agreement with previous results.¹⁰ The measured isotropic g-value is shown in figure 3.2d, with a measured g_{iso} value of 2.012. The line shape is best described as Lorentzian with a width (lwpp) of $\Delta B = 1.06$ G as measured from the highest-field line. This gives an approximate spin-spin relaxation value of $T_2 = 6.19 \times 10^{-8}$ s.

Figure 3.2. a) CW-EPR spectra of 100 μM of NITPh in distilled and de-aerated Toluene. b) The g_{iso} values of NITPh as calculated from the center inflection line of spectrum a. c) CW-EPR Spectra of 100 μM of IMIPh in distilled and de-aerated Toluene. d) The g_{iso} values of IMIPh as calculated from the center inflection line of spectrum c.



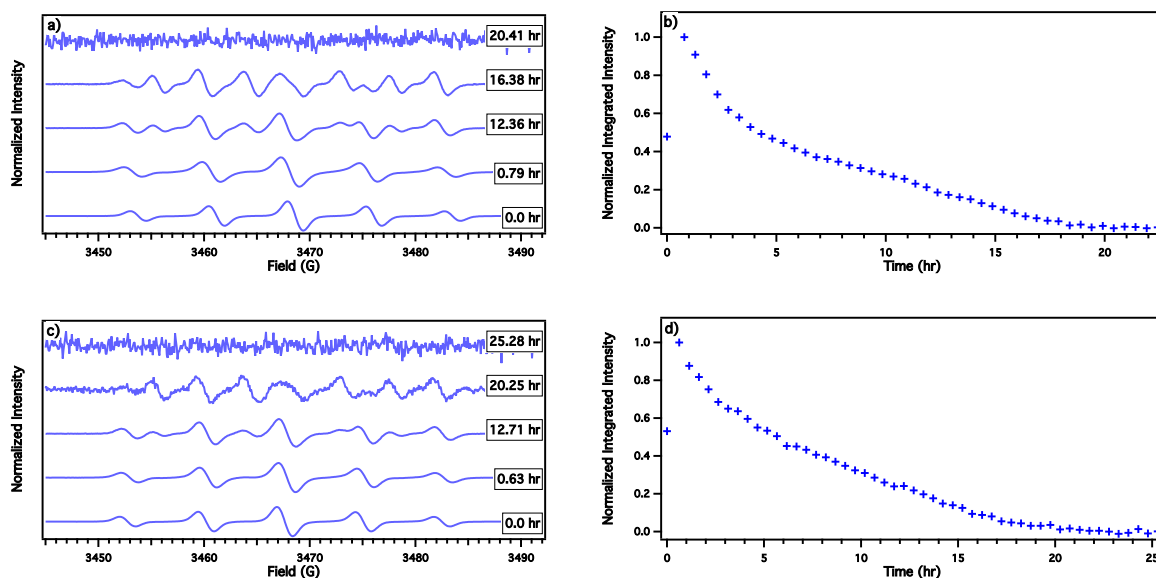


The results from the isotropic CW-EPR spectra of the pure NITPh and IMIPh radicals sets the baseline experiment for the next section, which examines the CW-EPR spectra of NITPh and IMIPh at two different concentrations, as well as when the radicals are mixed with CdTe QDs. Of particular importance are the changes in the pattern of the hyperfine structure.

Isotropic CW-EPR - NITPh/IMIPh and CdTe QD's. The CW-EPR spectra of 100 μM NITPh mixed with 1 μM CdTe ($D = 3.6$ nm) in de-aerated toluene is shown in figure 3.3a. The spectrum of NITPh at the 0.0 h time point represents 100 μM of NITPh prior to being mixed with the QDs. It displays a peak-to-peak line width $\Delta B = 1.33$ G and its shape is approximately Lorentzian. At the 0.79 h post mixing time point, the hyperfine structure becomes significantly broadened, with $\Delta B = 1.56$ G and it deviates significantly from its approximately Lorentzian shape. Line broadening continues for the first 10 hr after mixing, and for the first 3 h its shape is best characterized as being Gaussian. 10 h after mixing marks the point where the significantly broadened but characteristic 5-line pattern begins to split into a partially resolved 9-line pattern and the peak-to-peak line width of each hyperfine splitting gradually begins to decrease until it is lost into the background noise of the instrument. The signal intensity from the mixtures of 100 μM :1 μM NITPh/CdTe QD ($D = 3.6$ nm) becomes significantly broadened due to an unknown interaction with the CdTe QD system. As a result the calculations of the isotropic g-value, hyperfine splitting constant, and estimates of the spin-spin relaxation times (T_2) could not be made.

The normalized total integrated intensity of spectrum 3.3a is shown in figure 3.3b. At time 0 h the total intensity is approximately half ($I = 0.4783$) of the maximum-recorded intensity at time 0.79 h. The total intensity abruptly decreases over the course of 5 h and reaches its half-value $I_{1/2} = 0.5$ at time 4.27 h. After the first 5 h the rate of total intensity loss begins to decline until about the time 20.0 h, at which point the signal intensity is lost to the background noise of the instrument.

Figure 3.3. a) Room Temperature CW-EPR Spectra of 100 μM NITPh:1 μM CdTe ($D = 3.6$ nm) in de-aerated toluene. b) The normalized total integrated intensity of 100 μM NITPh and 1 μM CdTe ($D = 3.6$ nm) given in a. c) Room Temperature CW-EPR Spectra of 200 μM NITPh and 1 μM CdTe ($D = 3.5$ nm) in de-aerated toluene. d) The normalized total integrated intensity of 200 μM NITPh and 1 μM CdTe ($D = 3.6$ nm) given in c.



The CW-EPR spectra of 200 μM NITPh mixed with 1 μM CdTe ($D = 3.5$ nm) in de-aerated toluene is shown in figure 3.3c. At time 0.0 h, the solution consisting solely of NITPh displays a peak-to-peak width of $\Delta B = 1.31$ G and its shape is approximately Lorentzian. The splitting pattern at the 0.63 h time point is also significantly broadened, $\Delta B = 1.53$ G and deviates from a Lorentzian line shape. In addition to line broadening, a change in the hyperfine structure from a 5-line to 9-line splitting pattern is also observed. This takes place about 2 h

longer than was observed in the 100 μM NITPh mixture. As the signal intensity from the mixtures of 200 μM NITPh/1 μM CdTe QD ($D = 3.5$ nm) also becomes significantly broadened due to an unknown interaction, calculations of the isotropic g -value, hyperfine splitting constant, and estimates of the spin-spin relaxation times (T_2) could not be made.

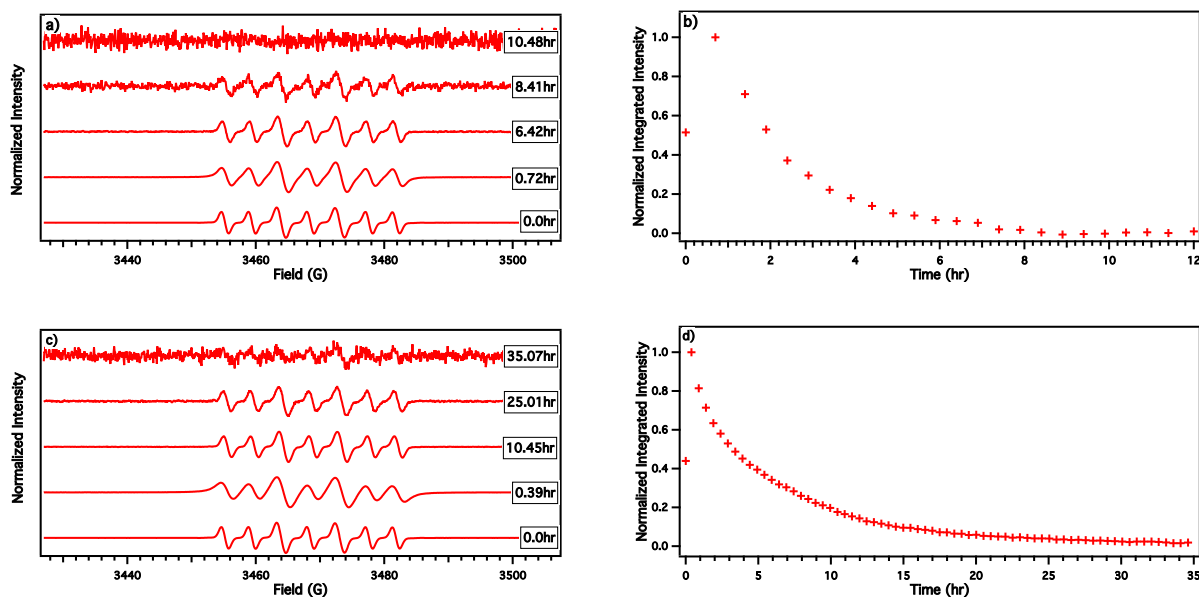
The normalized total integrated intensity of spectrum 3.3c is shown in figure 3.3d. At time 0 h the total intensity is approximately half ($I = 0.5312$) of the maximum-recorded intensity at time 0.79 h. The total intensity also abruptly decreases over the course of 6-7 h and reaches its half-value $I_{1/2} = 0.5$ at time 5.59 h. The pattern of total signal intensity decay occurs in this solution as well, but it takes approximately 5 additional hours for the signal to become lost in the background noise.

The CW-EPR spectra of 100 μM IMIPh mixed with 1 μM CdTe ($D = 3.6$ nm) in de-aerated toluene is shown in figure 3.4a. The spectrum of IMIPh at the 0.0 h time point represents 100 μM of IMIPh prior to being mixed with the QDs. Its peak-to-peak line width is $\Delta B = 1.02$ G and its shape is approximately Lorentzian. The splitting pattern at the 0.72 h time point becomes much more broadened, with a peak-to-peak width of $\Delta B = 1.64$ G and deviates from its approximately Lorentzian shape. Line broadening continues for the first 4 h after mixing and is best characterized as being Gaussian. After about 6 h the observed line broadening starts to reverse itself, and the peak-to-peak line width begins to narrow, at which point it gradually returns more Lorentzian shape. Unlike the spectrum of NITPh, the hyperfine splitting of IMIPh retains its characteristic 7-line pattern throughout all time intervals. Eventually the signal is lost into the background noise of the instrument. The signal intensity from the mixtures of 100 μM IMIPh/1 μM CdTe QD ($D = 3.6$ nm) becomes significantly broadened due to an unknown interaction, and although this reverses itself over the course of

approximately 6 h, calculations of the isotropic g-value, hyperfine splitting constant, and estimates of the spin-spin relaxation times (T_2) were not be made because of the lack of consistency amongst all time points.

The normalized total integrated intensity of spectrum 3.4a is shown in figure 3.4b. At time 0 h the total intensity is approximately half ($I = 0.4395$) of the maximum-recorded intensity at time 0.72 h. The total signal intensity steadily declines over 4 h time period, reaching a half value $I_{1/2} = 0.5$ at time 2.1 h. At approximately the 4 h time period point, the signal gradually declines and after 9 h the signal intensity is lost into the background noise of the instrument.

Figure 3.4. a) Room Temperature CW-EPR Spectra of 100 μM IMIPh and 1 μM CdTe ($D = 3.6$ nm) in de-aerated toluene. b) The normalized total integrated intensity of 100 μM IMIPh and 1 μM CdTe ($D = 3.6$ nm) given in a. c) Room Temperature CW-EPR Spectra of 200 μM IMIPh and 1 μM CdTe ($D = 3.4$ nm) in de-aerated toluene. d) The normalized total integrated intensity of 200 μM IMIPh and 1 μM CdTe ($D = 3.4$ nm) given in c.



The CW-EPR spectra of 200 μM IMIPh mixed with 1 μM CdTe ($D = 3.4$ nm) in de-aerated toluene is shown in figure 3.4c. At time 0.0 h, the solution consisting solely of IMIPh displays a peak-to-peak line width is $\Delta B = 1.10$ G and its shape is approximately Lorentzian. The splitting pattern at the 0.39 h time point is also significantly broadened, $\Delta B = 1.88$ G and it

also deviates from a Lorentzian line shape. As with the 100 μM solution, the hyperfine lines initially broaden until about the 10 h time point when they begin to slightly narrow. Due to a lack of consistency amongst all the time points, calculations of the isotropic g-value, hyperfine splitting constant, and estimates of the spin-spin relaxation times (T_2) could not be made.

The normalized total integrated intensity of spectrum of figure 3.4c is shown in figure 3.4d. At time 0 h the total intensity is approximately half ($I = 0.5312$) of the maximum-recorded intensity at time 0.39 h. The total intensity steadily decreases over the course of 20 h and reaches its half-value $I_{1/2} = 0.5$ at time 3.21 h. Eventually the total signal intensity decays into the background noise of the instrument, taking approximately 25 h for complete signal loss.

Although accurate and consistent measurements of T_2 could not reliably be obtained in this work, the changes in the hyperfine splitting pattern for both radicals over all time periods show no indication of surface binding with the CdTe QDs. Both nuclear spin active isotopes of Cd^{2+} , ^{111}Cd and ^{113}Cd carry approximately the same nuclear magnetic moment and quantum nuclear spin value ($I = 1/2$). For both NITPh and IMIPh radicals, the expected hyperfine splitting pattern from Cd^{2+} satellite features is up to 18 hyperfine lines. Although both lines are significantly broadened, a maximum of only 9 and 7 hyperfine lines are observed for NITPh and IMIPh respectively. However, it cannot be overlooked that the Cd^{2+} satellite features are unresolved and remain hidden in the observed broadening of hyperfine structure itself, particularly in the case of NITPh.

In addition to the absence of Cd^{2+} , surface binding of the radical to the CdTe should result in an increase in isotropic ^{14}N isotropic hyperfine constant. Due to the fact that line broadening may be caused by unresolved hyperfine structure, calculations of the ^{14}N isotropic hyperfine value for the radical/CdTe QD mixtures were not made in the work of this thesis. It

should be noted that increases in the isotropic ^{14}N hyperfine constant for both the nitroxide and imine nitrogen are expected to be small compared to their corresponding anisotropic values, whose measurements remain unfinished in this work. This is because most of the redistributed spin density upon coordination occurs in the planar p_z orbitals of the nitroxide and imine nitrogen.

A more useful measurement for deciphering the interaction of the radicals with the CdTe QDs is the decrease in the total area of the signal of each radical following their mixing. The total signal of both radicals rapidly declines until it can no longer be detected with instrumentation. Since the total signal is proportional to the radicals in the mixture, this indicates that the radicals are degrading over time as a result of a chemical reaction with either the CdTe QD itself or one of its surrounding ligands.

In the latter scenario a chemical reaction which destroys the radical seems more likely given that a twofold increase concentration of each radical, while holding the concentration of the CdTe QD constant, resulted in a longer time period for signal decay. For NITPh this corresponds to an additional 5 h. For IMIPh, this corresponds to an additional 25 h. While doubling the concentration of the radical should result in a proportional increase in the amount of time for observed signal loss, this is not observed here. The results remain ambiguous when comparing the times for half signal decay of each radical concentration. For NITPh this corresponds to an additional 1.32 h in going from 100 μM to 200 μM . Similarly for IMIPh, this corresponds to an additional 1.1 h in going from 100 μM to 200 μM .

The observed times necessary for total signal decay or for half signal decay are contradictory amongst the two concentrations of radicals used in this study. This might be explained by the chemical processes which must first occur at the CdTe QD surface in order to

react with each radical. These processes might include the desorption of the reactive native ligands surrounding the CdTe QD core, the adsorption of the radical ligands onto the reactive surface of the CdTe QD core, or a combination of both processes. This could explain the varying times for observed signal decay at each radical concentration. Insight into these processes was not pursued in this work.

However, based on previous knowledge regarding the chemical reactivity of nitroxide ligands, the most likely candidate responsible for the destruction of the radicals are the native phosphine ligands surrounding the CdTe QD surface. This is particularly true of trioctylphosphine, as triphenylphosphine is a known reducing agent of NITPh. The observed 9-line splitting pattern of NITPh over longer time intervals, may also be due to the presence of two or more radical species due to the above mentioned reasons. To test whether the phosphine ligands are primarily responsible for the degradation of the radical, a mixture consisting of 100 μM NITPh and IMIPh to 1 μM of CdTe QD in which the phosphine ligands surrounding the QD have been exchanged with octadecylamine. The results are discussed in the next section.

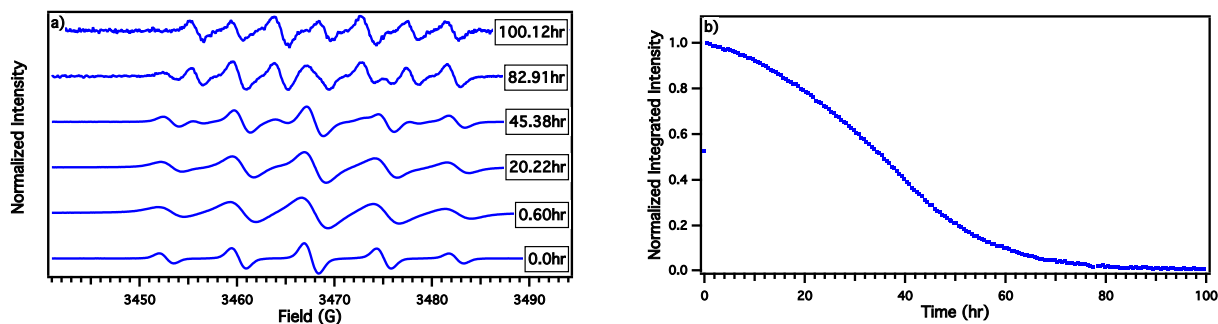
Isotropic CW-EPR - NITPh/IMIPh and CdTe QD's After Ligand Exchange

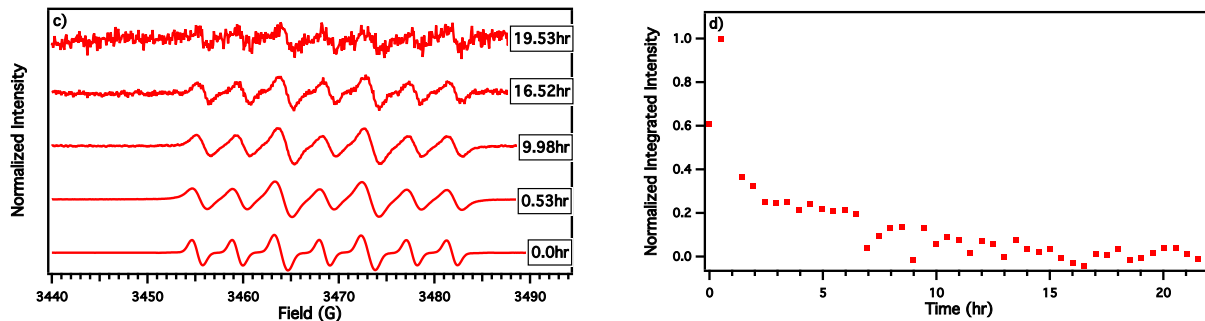
The CW-EPR spectra of 100 μM NITPh mixed with 1 μM CdTe ($D = 3.5\text{nm}$) whose native phosphine ligands have been replaced with octadecylamine are shown in figure 3.5a. The spectrum of NITPh at the 0.0 h time point represents 100 μM of NITPh prior to being mixed with the QDs. Its peak-to-peak line width is $\Delta B = 1.49\text{ G}$ and its shape is approximately Lorentzian. The splitting pattern at the 0.60 h time point becomes significantly broadened, with a peak-to-peak width of $\Delta B = 2.82\text{ G}$ and is almost Gaussian shaped. Line broadening continues for the first 45 h at which point the characteristic 5-line pattern begins to split into a partially

resolved 9-lines. The peak-to-peak line width gradually begins to decrease until it is lost into the background noise of the instrument.

The normalized total integrated intensity of spectrum figure 3.5a is shown in figure 3.5b. At time 0 h the total intensity is approximately half ($I = 0.5274$) of the maximum-recorded intensity at time 0.60 h. The total intensity steadily decreases over the course of 50 h and reaches its half-value $I_{1/2} = 0.5$ at time 3.21 h. After 50 h the signal decays at a slower rate, and after 100 h it is very weak. Data collection to complete signal decay was not possible due to instrumental complications at these longer time points. As a result of inconsistent line broadening and splitting patterns amongst the various time points, calculations of the isotropic g-value, hyperfine splitting constant, and estimates of the spin-spin relaxation times (T_2) were not be made.

Figure 3.5. a) Room Temperature CW-EPR Spectra of 100 μ M NITPh and 1 μ M CdTe ($D = 3.5$ nm) whose ligands have been exchanged with octadecylamine, in de-aerated toluene. b) The normalized total integrated intensity of 100 μ M NITPh and 1 μ M CdTe ($D = 3.5$ nm) given in a. c) Room Temperature CW-EPR Spectra of 100 μ M IMIPh and 1 μ M CdTe ($D = 3.5$ nm) whose ligands have been exchanged with octadecylamine, in de-aerated toluene. d) The normalized total integrated intensity of 100 μ M IMIPh and 1 μ M CdTe ($D = 3.5$ nm) given in c.





The CW-EPR spectra of 100 μM IMIPh mixed with 1 μM CdTe ($D = 3.5\text{nm}$) whose native phosphine ligands have been replaced with octadecylamine are shown in figure 3.5c. The spectrum of IMIPh at the 0.0h time point represents 100 μM of IMIPh prior to being mixed with the QDs. Its peak-to-peak line width is $\Delta B = 1.17\text{ G}$ and its shape is approximately Lorentzian. The splitting pattern at the 0.53 h time point becomes significantly broadened, with a peak-to-peak width of $\Delta B = 2.49\text{ G}$ and is Gaussian shaped. The characteristic 7-line splitting pattern is retained throughout all time points the initial broadening continues for the first 10 h, at which point the peak-to-peak line width begins to decrease until it is lost into the background noise of the instrument. The normalized total integrated intensity of spectrum 3.5c is shown in figure 3.5d. At time 0 h the total intensity is approximately half ($I = 0.6084$) of the maximum-recorded intensity at time 0.53 h. The total intensity steadily decreases over the course of 10 h and reaches its half-value $I_{1/2} = 0.5$ at time 1.10 h. After 10 h the signal intensity decays at a much slower rate, and after 16 h it is lost into the background noise of the instrument. As a result of inconsistent line broadening amongst the various time points, reliable calculations of the isotropic g-value, hyperfine splitting constant, and estimates of the spin-spin relaxation times (T_2) could not be made.

The results of the NITPh:CdTe mixtures after the native phosphine ligands have been exchanged with octadecylamine are similar to the results of the CdTe QDs with phosphine ligands. In the case of NITPh, the hyperfine lines broaden and then eventually split into a 9-line

pattern. They also broaden in case of IMIPh but they retain their characteristic 7-line pattern, which narrows at longer time periods. The time periods at which these events occur for IMIPh are similar in both phosphine and phosphine free CdTe QDs. The most significant contrast of this study is the amount of time it takes for the NITPh signal to decay and split into the 9-line pattern. This lends further evidence that an unknown chemical reaction involving the passivating ligands must first occur at the CdTe QD surface, prior to the observed chemical reaction. It may also indicate that NITPh must first be reduced to IMIPh before the radical is completely destroyed. It is possible that the complete removal of the phosphine ligands, such as TOP was not fully achieved with the ligand exchange procedure performed in this work. As discussed earlier in the introductory sections, while ^{31}P NMR remains a powerful tool for ligand exchange procedures, it is not a sensitive enough technique for the micro molar concentrations used in this study. Direct experimental evidence that NITPh follows a pathway where it is first reduced to IMIPh by TOP before it is destroyed was not pursued in this work.

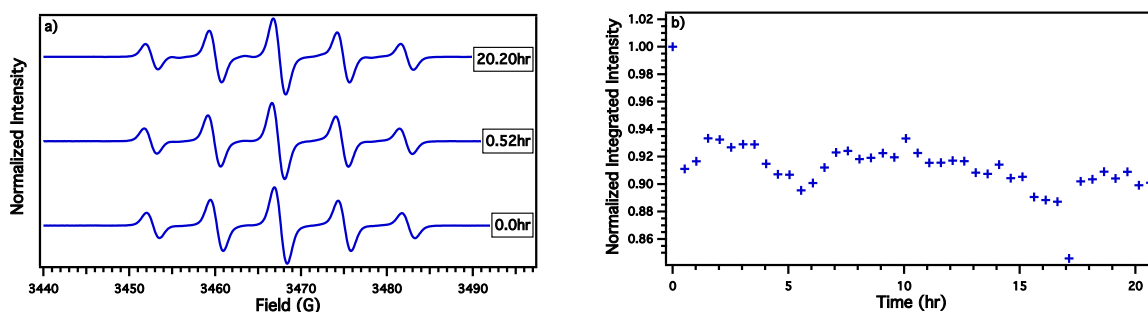
While the ligand exchange procedure most likely removed most of the phosphine ligands, ^{31}P NMR alone cannot rule out their complete absence from the CdTe surface. This is mainly due to the larger concentrations of sample needed to cause a NMR resonant signal. Since triphenyl phosphine is known to reduce NITPh to IMIPh, a mixture of NITPh and trioctylphosphine was prepared at a 1:1 (100 μM :100 μM) concentration.

The CW-EPR spectra of 100 μM NITPh mixed with 100 μM TOP in de-aerated toluene is shown in figure 3.6a. The 0.0 h time points peak-to-peak line width is $\Delta B = 1.47$ G and its shape is approximately Lorentzian. The same line broadening that occurs in the presence of the QDs does not seem to occur at the 0.52 h time point and its shape remains Lorentzian. The peak-

to-peak line width remains constant at $\Delta B = 1.47$ G for all time points of the study. After 20.2 h the spectrum is mostly unchanged, and NITPh keeps its characteristic 5-line hyperfine pattern.

The normalized total integrated intensity of spectrum 3.6a is shown in figure 3.6b. After mixing, the total intensity drops by about 10%, but then essentially remains constant throughout the remaining time points. The decrease total intensity may indicate that there is some reaction between NITPh and trioctylphosphine. This preliminary data suggests

Figure 3.6. a) Room Temperature CW-EPR Spectra of 100 μ M NITPh and 100 μ M trioctylphosphine in de-aerated toluene b) The normalized total integrated intensity of 100 μ M NITPh 100 μ M TOP given in a.



significant changes to the hyperfine structure are not observed at 1:1 concentrations. However, as can be observed from the data in figure 3.6b, there is significant oscillation arising from the instrument. This most likely arises from instability in the instruments magnetic field, microwave source, or a combination of both. Whatever the source, these instabilities prevents us from making a clear statement on the effects of TOP on NITPh.

3.4 Conclusion

In this work, the interaction of both NITPh and IMIPh with two types of CdTe QDs were examined. In the first CdTe QD system studied, the surface ligands surrounding the QD core were primary composed of native phosphine ligands, namely trioctylphosphine and trioctylphosphine oxide. In the second CdTe QD system studied, these native phosphine ligands were removed as was determined by detectable limit of ^{31}P NMR spectroscopy.

A clear interaction between the CdTe QDs surrounded by native phosphine ligands and NITPh occurs at both concentration regimes was observed. In both concentration regimes, dramatic changes in the hyperfine structure occurred over long periods of time. In addition, the total signal intensity is also lost over time. This lends strong evidence to the fact that an unknown chemical process involving either the reactive surface of the CdTe QD, its phosphine ligands, or a combination of the two are responsible for degrading NITPh. The changes in the hyperfine interaction for the NITPh radical may indicate that two or more radical species may exist as a result of this process. While the existence of surface binding cannot be conclusively ruled out, it seems unlikely given that Cd^{2+} satellite features are not observed. However, the significant line broadening observed for NITPh could overshadow the satellite features in the hyperfine signal.

The interaction between CdTe QDs surrounded by native phosphine ligands and IMIPh at both concentrations is less clear. The hyperfine structure at both concentrations does not change appreciably over the time intervals studied, and while it initially broadens it begins to narrow while still deviating from its original Lorentzian shape. In both concentration regimes studied, Cd^{2+} satellite features are not observed and the total signal intensity is lost over long periods of time. This lends strong evidence to the fact that an unknown chemical process involving either the reactive surface of the CdTe QD, its phosphine ligands, or a combination of the two are responsible for degrading the radical nature of IMIPh.

The results from the CdTe QDs whose surfaces are passivated by phosphine ligands mirror the results of the same QDs that underwent a ligand exchange treatment, where the phosphine ligands were replaced by octadecylamine. Namely, the changes in the hyperfine pattern for NITPh gradually change from a 5-line to a 9-line pattern the studied time intervals

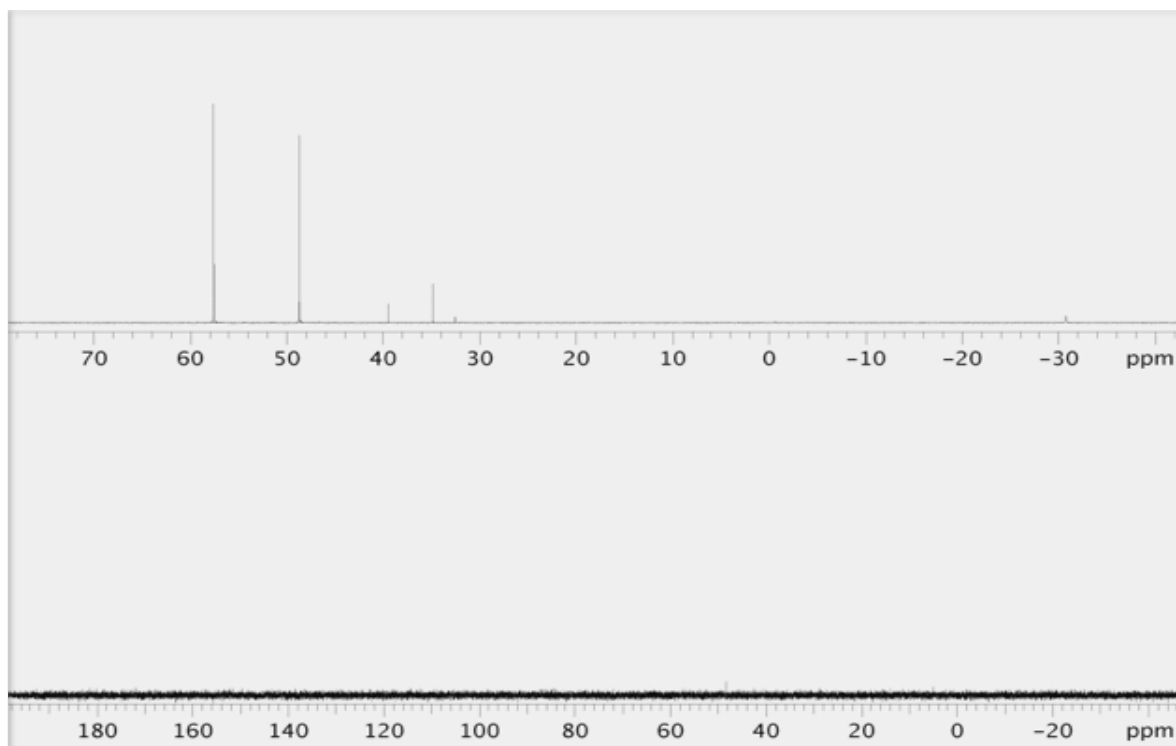
while IMIPh retains its characteristic 7-line pattern. Over the time intervals studied the total signal intensity of both radicals is lost. The biggest contrast between the two different types of CdTe QDs and the two radicals studied is the longer amount of time necessary for total signal loss of NITPh. This may be due to an unknown reaction mechanism involving the surface of the quantum dot, the octadecylamine, or both.

Comparing the results from the NITPh and trioctylphosphine study to the study of CdTe QDs with phosphine ligands seems ambiguous at the time of this work. While the radical retains its characteristic 5-line hyperfine pattern throughout all time intervals, the signal intensity is only decreased about 10% approximately 0.5 h after mixing. Furthermore observing any conclusions regarding the reaction of NITPh and TOP are obstructed by instabilities in instrumentation.

APPENDIX

Appendix

Figure A.1. ^{31}P NMR spectra of a 1.5 mM stock solutions of CdTe ($D = 3.5$ nm) prior too (top) and following (bottom) the ligand exchange procedure.



The top of figure A.1 shows both free and bound phosphine ligands (TOP and TOPO), which have been removed beyond the detection limit of ^{31}P NMR. As discussed earlier this does not preclude the possibility that these phosphine ligands still exist at micro molar concentration range. Experimental parameters: solvent = CDCl_3 , spectral width = 50,000 Hz, acquisition time = 0.655 s, data points = 32,768, relaxation delay = 5s, pulse angle = 45° , number of scans = 64.

Figure A.2. Normalized Absorbance spectra of CdTe ($D = 3.5$ nm) prior too ($14.5 \mu\text{M}$ - red) and following (500 nM - blue) the ligand exchange procedure.

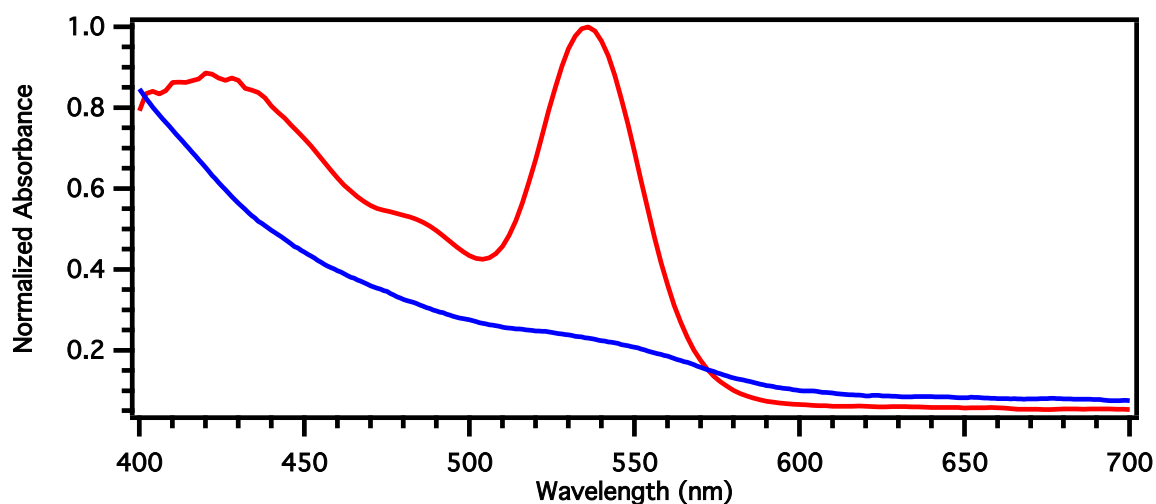


Figure A.2 shows the same samples of CdTe prior too and following the ligand exchange procedure. The comparative spectra were normalized because concentrations of the two samples could not be held constant in order to conserve the post ligand exchange aliquot for the EPR-Radical studies. The main features of the post ligand exchange sample are the increased size distributions of the CdTe QDs as a result of the procedure. This increased size distribution observed in the CdTe QDs could have had a contributing effect on the observed increase decay time of both radicals, however this was not addressed at the time of this work.

LITERATURE CITED

LITERATURE CITED

1. Wagner, B. E.; Helbert, J. N.; Bates, R. D.; Poindexter, E. H., Spin density delocalization from a stable free-radical ligand onto diamagnetic metal ions. *Journal of the Chemical Society, Chemical Communications* **1973**, 19, 748-749.
2. Semmelhack, M. F.; Schmid, C. R.; Cortes, D. A.; Chou, C. S., Oxidation of alcohols to aldehydes with oxygen and cupric ion, mediated by nitrosonium ion. *Journal of the American Chemical Society* **1984**, 106, 3374-3376.
3. Takaya, Y.; Matsubayashi, G.; Tanaka, T., Reactions of 2,2,6,6-tetramethylpiperidine nitroxide radical with Tin(IV) halides. *Inorganica Chimica Acta* **1972**, 6, 339-342.
4. Dickman, M. H.; Doedens, R. J., Structure of chloro(2,2,4,4-tetramethylpiperidinyl-1-oxo-O,N)(triphenylphosphine)palladium(II), a metal complex of a reduced nitroxyl radical. *Inorganic Chemistry* **1982**, 21, 682-684.
5. Ullman, E. F.; Osiecki, J. H.; Boocock, D. G. B.; Darcy, R., Studies of Stable Free Radicals. X. Nitronyl Nitroxide Monoradicals and Biradicals as Possible SmallMolecule Spin Labels. *Journal of the American Chemical Society* **1972**, 94, 7049-7059.
6. Golubev, V. A.; Zhdanov, R. I.; Gida, V. M.; Rozantsev, É. G., Reaction of iminoxyl radicals with triphenylmethylcarbonium salts. *Russian Chemical Bulletin* **1970**, 19, 2651-2653.
7. Nagy, V. Y.; Petrukhin, O. M.; Zolotov, Y. A., Application of Stable Radical-Containing Complexing Reagents for the ESR Determination of Metals. *C R C Critical Reviews in Analytical Chemistry* **1987**, 17, 265-315.
8. Caneschi, A.; Gatteschi, D.; Laugier, J.; Rey, P.; Zanchini, C., Synthesis, x-ray crystal structure, and magnetic properties of two dinuclear manganese(II) compounds containing nitronyl nitroxides, imino nitroxides, and their reduced derivatives. *Inorganic Chemistry* **1989**, 28, 1969-1975.
9. Tretyakov, E. V.; Romanenko, G. V.; Ovcharenko, V. I., Syntheses and structures of azol-1-yl derivatives of nitronyl and imino nitroxides. *Tetrahedron* **2004**, 60, 99-103.
10. Boocock, D. G. B.; Darcy, R.; Ullman, E. F., Studies of Free Radicals. II. Chemical Properties of Nitronyl Nitroxides. A Unique Radical Anion. *Journal of the American Chemical Society* **1968**, 90, 5945-5946.

Chapter 4

Conclusion

This thesis has focused on the synthesis and characterization of two nitroxide radicals, the nitronyl nitroxide radical NITPh and the imino nitroxide radical IMIPh. In addition the synthesis and characterization of CdTe QDs was also presented. Both nitronyl and imino nitroxide radicals have previously been used as ligands for a variety of metal nitroxide complexes. Most of these complexes were studied for the use as potential organic inorganic hybrid molecular magnets, as a most of the metals in these coordination complexes are paramagnetic. However, in a few cases both radicals have been used as spin probes for studying diamagnetic metal complexes. In these studies, EPR spectroscopy was mainly used to assess the electronic changes that occur to the nitroxide radical ligands as a result of complex formation.

This work attempted to use NITPh and IMIPh as spin probes in a similar manner, namely for studying the binding interactions of both radicals to the surfaces of CdTe QDs. EPR spectroscopy was the fundamental characterization technique of these studies. In the work of this thesis, the binding interaction of both radicals to the surface of the CdTe QDs was not observed. While the changes in the EPR spectrum are indicative of a changes in the structure of the radicals, the more probable explanation for the results of this work; is that the radical undergoes a chemical reaction with the surface of the CdTe QD, its surrounding ligands, or a combination both the surface of the QD and its surrounding ligands.

While the exact mechanism by which the radical is destroyed by CdTe QD remains unknown, the ligand exchange studies seem to implicate the native phosphine ligands as the likely candidate. This is particularly true of the NITPh radical, where the ligand exchange experiment resulted in a dramatic increase in the time for total signal loss. Further evidence

supporting the role of phosphine ligands in the destruction of the radical, comes from previously known reactivity of NITPh with triphenylphosphine. However, the results of the trioctylphosphine and NITPh mixture do not necessarily support this conclusion. In addition, a significant increase the time necessary time for total signal intensity decay for IMIPh and CdTe QDs in the post ligand exchange experiments, is not appreciably longer than the experiments performed on the CdTe QDs with phosphine ligands. This may indicate the surface of the CdTe QD itself plays a role in the destruction of both radicals, and may even involve a surface catalyzed reaction between the ligands and radicals.

While the results from this thesis are mostly exploratory, there is a lot of work to be done in elucidating the mechanism responsible for the destruction of the radical by CdTe QDs. Although every attempt was made to remove the phosphine ligands from the CdTe QDs, it is likely that they were not completely removed using the ligand exchange technique employed in this work. To ensure that CdTe QDs are completely free of phosphine ligands requires a new synthetic approach using phosphine free native ligands during synthesis and for post synthetic treatments. This could possible elucidate any catalytic surface interaction of CdTe QDs towards the radicals.

In addition to the chemical reactivity of the CdTe QDs towards the nitroxide ligands, the binding interactions of both radicals to the surfaces of QDs should not abandon based on the results of this work. As stated earlier, nitroxides are extremely weak Lewis bases. While the imine nitrogen in imino nitroxide radicals acts a stronger Lewis base toward metal center, accessibility towards coordination at this site is most likely strained due to the bulky constituent groups attached to the radical. This is most likely true of the phenyl constituent group used in this study. Future surface binding studies of radical spin probes may find better success if the

constituent groups of each radical are varied so that they themselves carry stronger coordinating functional groups.